PhD degree in System Medicine

European School of Molecular Medicine (SEMM)

University of Milan

AN ELECTROCHEMICAL MICROFLUIDIC BIOSENSOR PLATFORM FABRICATED BY ADDITIVE MANUFACTURING AND SUPERSONIC CLUSTER BEAM DEPOSITION

Wondimu Alemu Gebreyes

Centro Interdisciplinare Materiali ed Interfacce Nanostrutturati – CIMAINA

Matricola n. R11156

Supervisor: Prof. Paolo Milani

Dipartimento di Fisica – Università degli Studi di Milano

Abstract

In integrated electrochemical microfluidic biosensors, the synergy between control over fluids in a miniaturized environment and electrochemical detection on thin films microelectrodes enables the development of microfluidic Lab-on-Chip (LOC) biosensors with enhanced sensitivity and selectivity, disposability, reduced cost, portability, real-time detection, and high throughput. Because of these advantages, several attempts have been made to develop rapid prototyping methods for producing integrated microfluidic biosensor platforms using polymeric materials. Recently, Fused Filament Fabrication(FFF) additive manufacturing, which is based on the layer by layer deposition of thermoplastic melt extrusion attracted much attention for the fabrication of microfluidic platforms in a single step, with high process speed, low production costs, and automated manufacturing directly from virtual data. However, because of the poor adhesion between metallic thin film electrodes fabricated using conventional techniques and FFF printing materials electrodes are usually integrated into microfluidic platforms either modularly or using adhesive layers placed at the bottom of the fluidic channels. This hinders exploitation of the huge potential of such rapidly expanding FFF technology for scale-up manufacturing of integrated microfluidic biosensors. In this Ph.D. work, supersonic cluster beam deposition(SCBD) technology was employed for the successful fabrication of nanostructured thin film electrodes directly integrated into FFF printed microfluidic platforms.

SCBD enables the formation of strongly anchored metallic thin films by implanting supersonically accelerated neutral metal clusters into any polymeric substrate. The SCBD technology enables depositing over large areas by using a variety of materials, such as noble metals and metal oxides, with precisely controlled surface topography that determines the deposited film wettability, isoelectric point, and biocompatibility, that would in turn tailor the loading and physical adsorption of biological molecules to enhance the performance of biosensors. A novel integrated manufacturing approach was developed and optimized in order to couple the two additive layered manufacturing methods, SCBD and FFF 3D printing for the fabrication of electrochemical microfluidic platforms provided with electrodes employed for Lab-on-chip electrochemical biosensors. Consumer-grade FFF printed fluidic thermoplastic microfluidics with channels having different dimensions, fluidic ports and electrical interconnections, employing acrylonitrile butadiene styrene (ABS) as the base material was monolithically integrated with SCBD deposited Au-working, Au-counter and Ag/AgCl reference electrodes to develop a three electrodes configuration electro-chemical cell on-chip. The potential functionality of the prototype of the three-electrodes embedded electrochemical microfluidic biosensors as electrochemical sensors was assessed employing cyclic voltammetry, chronoamperometry and electrochemical impedance spectroscopy measurements performed in stagnant ferrocyanide-ferricyanide redox solution. The cyclic voltammetry response showed that the prototype possessed huge functionality for electrochemical detection and analysis. The chronoamperometry measurement indicated the electrode embedded microfluidic platform enabled highly sensitive detection of the probe. The elec-

trochemical impedance spectroscopy revealed that the embedded electrode possessed highly rough and porous surface features that enhance sensitivity and detection range. In addition, the in-channel flows dynamic cyclic voltammetry recorded in the same probe with various flow rates resulted in increased Faradic current that signifies the potential to improve sensitivity and enhances the detection limit of the sensors. Thus, leveraging the novel integration approach the SCBD and FFF technologies can be integrated to manufacture highly sensitive, low-cost, portable and user-friendly electrode embedded electrochemical microfluidic biosensors. The device could be readily employed for various customized clinical, industrial, and environmental sensing applications.

Acknowledgement

I am deeply indebted to my supervisor Professor Paolo Milani for giving this PhD opportunity, providing continuous support and guidance and for his patience throughout my 4 years stay at the Physics department of the university of Milan.

I also would like to sincerely thank Dr.Tommasso Santaniello for supporting me throughout the PhD work, taking care of the city registration from the beginning, giving prerequisite training and enabling me to quickly blend into the scientific community.

I acknowledge the support of Mr.Daniele Maria Vigano and Federico Pezzota, members of the physics department workshop for providing technical training, producing masks and supplying materials whenever needed during the entire process.

My sincere thank goes to electrochemistry group of the Tel Aviv University, Professor Yosi Shacham team for providing training on electroplating, electrochemical characterization methods and silver electroplating bath with protocols used for fabrication of Ag/AgCl quasi-reference electrode.

I sincerely thank Dr. jinlong Yin at Teer Coatings Ltd, Droitwich-UK for

providing me with advanced practical training on magnetron based cluster assembled nanostructure deposition, and PVD(magnetron sputtering) when I went to this company for secondment.

I am very grateful to two Ph.D. students Lorenzo Migliorini and Chloè Minnai for depositing metallic thin films that were used in this project employing SCBD .

I would also like to thank FP7 - Marie-Curie Initial Training Network for young researchers in nanotechnology for funding my entire expenses leading to this Ph.D. results. The program provided me with excellent laboratory training, several summer schools and other training organized by Catsense member universities, companies, and research laboratories. It was a great privilege to be a part of the Catesense project.

I am grateful to all scientific and technical staff members of the physics department at Centro Interdisciplinare Materiali ed Interfacce Nanostrutturati – CIMAINA.

I would like to express my sincere gratitude to my mother Abebech Tsegay who has been my idol and inspiration after my father passed away while I was in junior secondary school.

Contents

List of Figures

List of Tables

Chapter 1

Introduction

Electrochemical microfluidic biosensors have emerged as a powerful technique in chemical and biological detection and analysis [1, 2, 3]. They retain a huge potential application in health cares [4, 5], water and food quality assurances [6, 7, 8], agriculture [10, 11], and environmental monitoring [12, 13, 14, 15] because of their advantages of simplicity, higher sensitivity and selectivity, disposability, portability, and cost-effectiveness [16]. For the last three decades, electrochemical microfluidic biosensors have revolutionized traditional detection and analysis into the point of care testing, and rapid and onsite real-time monitoring system. This created an unprecedented promising opportunity for patients and physicians to get real-time feedback information about the patient [17, 18, 19], real-time detection for clinical studies [21] and in situ investigation of environmental condition [22, 23]. Among many commercially available portable electrochemical biosensors, home blood glucose monitoring used to assist diabetes in controlling their blood glucose level [24], and I-stat blood analyzer [25] are typical examples.

Currently, electrochemical biosensors represent the most rapidly developing class of sensors and captures the largest market share among thermal, piezoelectric, and optical biosensors [26, 27]. Driven by increasing diabetes population, a prevalence of lifestyle associated diseases, and increasing application of biosensors in various industries, global electrochemical biosensors market is projected to reach USD 23707.2 million by 2022 and the biosensors industry is expected to grow at a CAGR of 9.6% by the forecasted years [28].

During the last two decades the marriage between electrochemical biosensors and microfluidics technology enabled by advancement of nanofabrication technology facilitated integration of electrochemical and biological units into the microfluidics platform consequently engendering microfluidic Lab-on-Chip (LOC) biosensors with improved sensitivity, selectivity, disposability, reduced cost, portability, real-time detection and high throughput [29, 30, 31, 32, 33]. Due to such advantages several extensive types of research have been conducted to develop new nanomaterials transducers [34, 35, 36, 37, 38, 39, 40], novel fabrication strategies [41, 42, 43, 44, 45], and versatile and low-cost base materials [46, 47, 48, 62, 50, 51, 52, 53, 54, 55] for building microfluidics platform in order to develop faster prototyping methods with reduced cost, enhanced performance and portability.

Despite significant signs of progress, abundant manufacturing of microfluidic LOC electrochemical biosensors have been impeded because conventional microfabrication approaches which are adapted for polymer-based microflu-

idics rely on the use of expensive techniques (e.g. injection molding, casting, embossing)[56, 57] or time-consuming methods (e.g. laser writing [58], electron beam lithography [59]). Furthermore, a multistep production process for the assembly and sealing of the systems of different components after the electrodes fabrication (e.g. via adhesive or thermal bonding) is required, and hence these strategies are inefficient for prototyping[60]. Moreover, it is also significantly constrained by the interplay between the choice of microfluidics base materials and compatibility of transducer fabrication tools [61, 62]. This is due to the requirement that the microfluidic biosensor platform must be biocompatible to accommodate bioreceptors and simultaneously exhibit a strong adherence for thin film electrodes [63]. Soft lithography using PDMS elastomers and thermoplastics polymers have transformed the fabrication process into a cheaper and benchtop process [64, 65] however, the electrochemical microfluidic biosensors have remained only in routine laboratory research works.

Recently, layered additive manufacturing (or 3D printing technology) has become increasingly popular for prototyping (RP) of microfluidic biosensors because of the huge capability of these methods to produce the device in a layer-by-layer fashion directly from digital models, in a single step with low cost, enhanced pace and automated systems [66, 67, 68, 69, 70]. However, their full potential for building unitarily microfluidics integrated electrochemical biosensors have not been exploited due to the incapability of the existing fabrication tool to directly deposit a strongly anchored functional electrochemical transducers onto RP printed polymer substrates, requisite

for building cost-effective sensors. This precluded efficient use of the three-dimensional printing technology for manufacturing scale-up of microfluidics integrated electrochemical biosensors.

The SCBD produces strongly anchored nanostructured thin film with tailored morphology from gas phase cluster sources [71, 72] on various substrates including thermoplastic polymers [73, 74, 75]. It allows deposition of large area metallic thin films at room temperature enabling deposition on temperature sensitive substrates. In this project, SCBD was leveraged to couple with FFF technology employing a novel fabrication strategy to develop unitarily electrode integrated microfluidics electrochemical sensor platform with an improved fabrication pace, low cost, portability, and autonomy. This Ph.D. project focused on three primary areas to fill the gap needed to bring RP technology, particularly FFF technology for developing fully integrated electrochemical microfluidics biosensor device.

In the first part potential application of SCBD fabricated nanostructured material directly depositing on thermoplastic FFF printed materials from gas phase cluster source were assessed for potential to build electrochemical devices. In this case, the nanostructured materials were used as an electrochemical transducer and complementary electrodes to establish an electrochemical cell. By depositing the nanostructured materials directly on FFF printed substrates, the SCBD opens up a way to bring the FFF technology for application in the fabrication of electrode embedded electrochemical microfluidics biosensors. The large area deposition capability the SCBD tech-

nology enables fabrication of fully functional microfluidics integrable working and counter electrodes.

In the second part, metalization capacity of the SCBD technology was employed to bridge FFF technology and electroplating methods to fabricate Ag/AgCl quasi-reference electrodes. In this case, the FFF printed thermoplastic materials became metalized using SCBD by implantation of metallic nanoparticles into the polymer matrix [73], which was subsequently used as conducting path to electrodeposition of functional and microfluidics integrable quasi-reference electrodes [74, 75].

The third part focused on developing a novel integration strategy to combine the SCBD deposited electrodes and FFF printed microfluidics platform to develop the integrated device. In addition, relevant surface treatment technique was studied to improve the poor surface finish inherent to FFF printed materials [76, 77]. The electrode embedded electrochemical microfluidic biosensors platform was successfully developed as a proof of concept, which can be readily customized for building various electrochemical microfluidic integrated biosensor devices.

The first chapter of this report presented the general introduction and motivation. The aim of the Ph.D. project was described in chapter two. The third chapter discussed relevant background on electrochemical biosensors, applications of nanostructured materials in electrochemical biosensors, basic components of electrochemical sensors, and microfluidics integrated biosen-

sors. Materials and methods used to accomplish this project was reported in the fifth chapter. This chapter also discussed the experimental procedures executed to accomplish the proposed device. The fifth chapter presented results and discussions. Summary of the project and future perspective was presented in this chapter.

Chapter 2

Aim of the project

The aim of this Ph.D. project was to develop a quick, inexpensive and scalable rapid prototyping mechanism integrating FFF and SCBD for manufacturing of electrode embedded electrochemical microfluidic biosensor platform, which is highly sensitive, portable, and user-friendly. For realization of the device, the ability of SCBD technology to fabricate strongly anchored large area metallic thin film with tailored surface morphology from gas phase cluster source and the huge capacity of FFF technology to manufacture a microfluidic device directly from virtual data were exploited by bridging through a novel integration strategy.

The viability of the proposed platform for electrochemical sensing application was demonstrated by constructing the device by embedding three electrodes electrochemical cell, the SCBD manufactured Au working and counter electrodes, and electroplated Ag/AgCl quasi−reference electrode into FFF fabricated microfluidic platform and then electrochemically characterizing in

ferro/ferricyanide redox couple using cyclic voltammetry, amperometry, and electrochemical impedance spectroscopy. Moreover, the potential application of the prototype for online or dynamic flow sensing was assessed by recording flow cyclic voltammetry in ferro/ferricyanide flowing through the channel passed the surface of embedded electrodes with various flow rate.

In summary, four research goals are formulated in this project: Investigation of the SCBD technology potential for deposition of nanostructured electrode materials on FFF printed thermoplastic polymers that could be employed for manufacturing of electrochemical biosensors. In addition, exploit the plastic metalization capacity of the SCBD for fabrication of microfluidics integrable Ag/AgCl quasi-reference electrode.

Developing surface modification methods that reduce the poor surface finish of FFF printed materials in order to use for building a platform suitable for fabrication of electrode materials.

Developing a novel fabrication strategy to integrated FFF and SCBD technology to manufacture electrode embedded electrochemical biosensors.

Electrochemical evaluation of the integrated platform potential application as a sensor.

Chapter 3

Background

3.1 Electrochemical Biosensors

According to IUPAC 1999 definition an electrochemical biosensor is defined as a self-contained integrated device, which is capable of providing specific quantitative or semi-quantitative analytical information using a biological recognition element which is retained in direct spatial contact with an electrochemical transduction element.[78]

Fig. 3.1 shows typical electrochemical biosensor parts. a) The bioreceptors such as enzymes, antibodies, DNA, antigens, whole cells, tissues, plant and various synthetic molecules that interact with analyte through affinity or catalytic bonding. b) A transducer that serves as a bioreceptor immobilization platform and converts biochemical signal resulting from the interaction of the analyte with the bioreceptor into an electronic signal. c) The electrochemical excitation signal is delivered and the response is recorded and

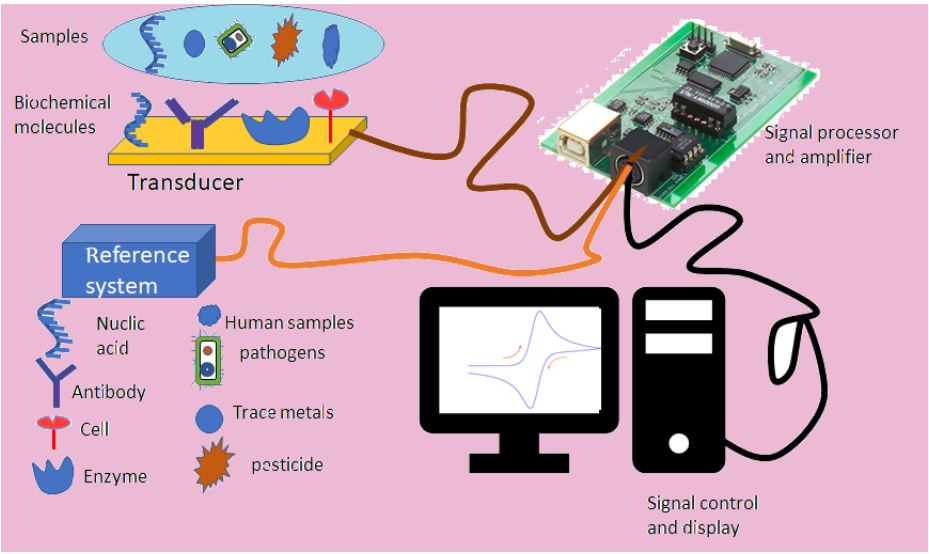

Figure 3.1: Basic components of electrochemical biosensors

processed by the potentiostat. Then the response was converted to meaningful information by a computer software. The generated signal is proportional to the analyte concentration.

The basic principle of electrochemical biosensors rely on interfacial charge distribution and transfer dynamics between an electrode and an analyte in a solution. The charges are generated from the electrochemical reaction at the electrode surfaces. This charge distribution or transfer can cause a flow of current, generates voltage or causes a change in impedance of the electrochemical system that can be modulated by applying an external signal. The produced electrical signals can be correlated with either the concentration of electroactive species present in the solution or its rate of production or consumption, which is proportional to the analyte concentration [79].

3.1.1 Electrochemical cell

All electrochemical biosensors are composed of three electrode electrochemical cell to prompt interface electrochemical reaction, facilitate charge transfer process and record the response. The charge transfer process between the electrode and solution near the interface is induced by applying an external potential to conform the Fermi level of the electrode such that it matches with molecular orbitals of the electroactive species in the solution as shown in Fig.3.2. In this case, the HOMO/LUMO energy levels correlate with the formal potential of the electroactive redox couples, and the electrode potential at chemical equilibrium is given by the Nernst equation 3.1 [80].

$$E_e - E^o = \frac{RT}{nF} \ln \frac{[Ox]}{[Red]} \tag{3.1}$$

E_e is the electrode potential, and E^o is the formal potential, R is the gas constant (8.314 J K^{-1} mol^{-1}), T is the system absolute temperature (K), F is the Faraday constant (96,485 C mol^{-1}) and [Ox] and [Red] are concentration of oxidized and reduced species respectively.

When overpotetnial is applied to give rise redox electrochemical reaction, the electrochemical kinetics is governed by the Butler-Volmer equation. The fundamental relationship between current and applied potential is given by

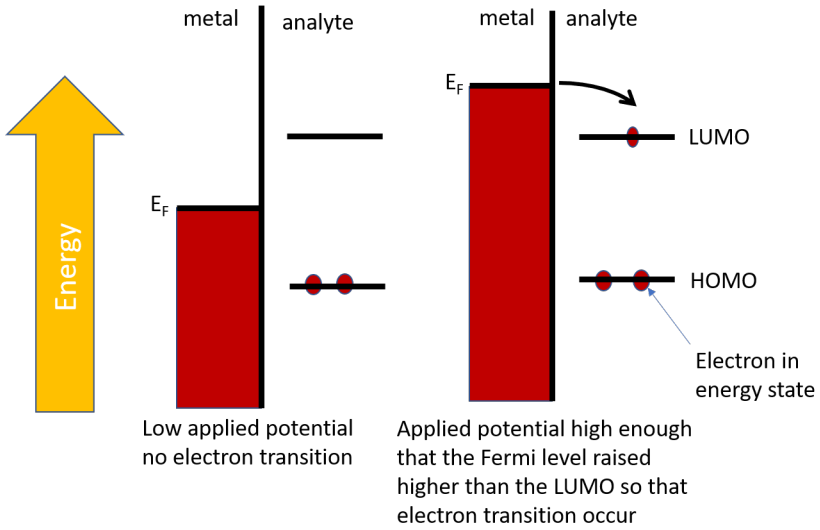

Figure 3.2: Fermi level adjusting for reduction of analytes

the equation 3.2 [80].

$$i = i_o[\exp(-\frac{\alpha nF}{RT})(E - E_o) - \exp\frac{(1-\alpha)nF}{RT}(E - E_o)] \tag{3.2}$$

Here, where i_o is exchange current density, E_o (in V) is the standard potential of the redox reaction, E (in V) is the applied potential, R is the gas constant (J/K mol), F is the Faraday constant (C/mol), T (in K) is the temperature, n is the number of electrons transferred, α and is the transfer coefficient.

The simplest conventional electrochemical cell is shown in Fig. 3.3 contains a working electrode, counter electrode, and reference electrode. In this set up the external potential that give rise redox reaction is applied to work-

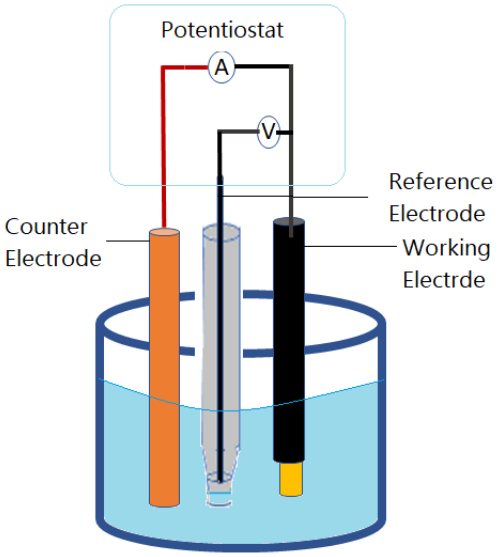

Figure 3.3: Simple conventional electrochemical sensor

ing electrode with respect to the reference electrode. The resulting current from the redox reaction is measured between the working and counter electrodes.

The working electrodes are the most important part of the electrochemical cell, which serves as a biochemical element immobilization platform and at which an electrochemical reaction occurs. The choice of the working electrode is often based on signal-to-noise ratio, reproducible response, free of interfering reactions over the potential of interest, high electrical stability, low cost, biocompatibility, and long-term stability, potential window, better electron transfer efficiency, high bioconjugation efficiency, and favorable redox property. Usually, the working electrode is made of Au, Ag, Pt, Hg drop and film and glassy carbon etc. The counter electrode is used to complete

a circuit of three-electrodes electrochemical cell established to measure current resulting from an electrochemical reaction. The most commonly used counter electrode materials include inert material (e.g. Pt, Au, graphite, glassy carbon) and silver [81].

Reference electrode provides stable potential against which the potential of the working electrode is controlled and measured, is kept at a distance from the reaction site. Among commonly used reference electrodes such as Hg/Hg_2Cl_2 (calomel) and the standard hydrogen electrode(SHE), AgCl is widely used because it is easy and cheap to prepare, simple, relatively non-toxic, possess huge prospect of miniaturization and integration with the existing technologies [82, 83, 84]. The typical potential of the Ag/AgCl half-cell reaction shown in equation 3.3 is determined by the chloride concentration of the solution [85].

$$AgCl <-> Ag(s) + Cl^-_{aq} \qquad E_o = +0.222VVs.SHE \tag{3.3}$$

At the interface of the electrochemical cell and solution, there is the formation of an electric double layer (EDL) depicted by the model shown in Fig. 3.4. The first region consists of a charged solid surface and a net excess of hydrated counter-ions. This region is compact charged layers made up of parallel charge layer of the electrode surface and hydrated opposite ions. It is represented by parallel plate capacitor [80]. The stern layer represents immobile hydrated counterions adsorbed to the electrode and immediately adjacent to the wall. The diffuse and mobile layer separated by shear plane from

the Stern layer is designated by Gouy-Chapman Layer. This interface phenomenon provides information about electrode reaction kinetics that enables to assess the surface property and conductivity, criteria on which electrode material selection is based on, and the proper immobilization of biochemical molecules.

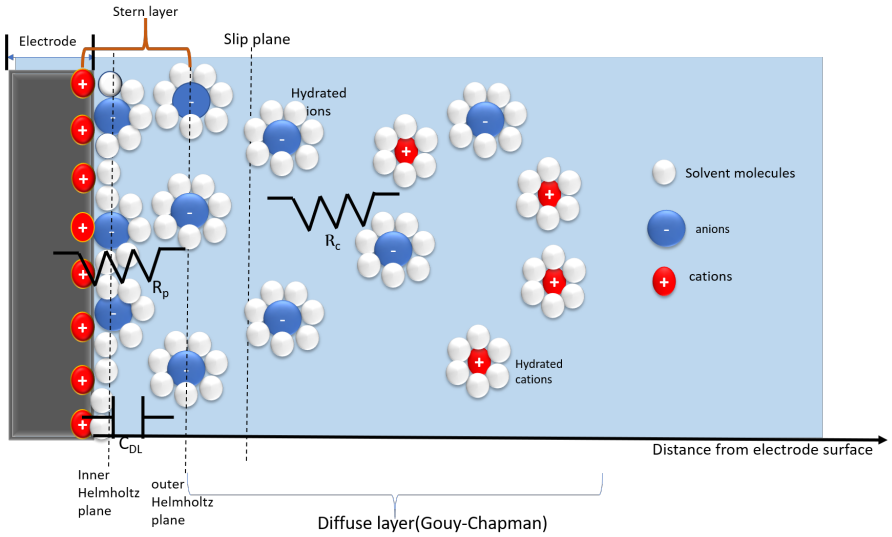

Figure 3.4: Electrochemical interface

3.1.2 Nanostructured thin film Electrodes

The cost, performance, and portability of electrochemical biosensors have improved with the advancement in the synthesis of nanostructured materials(NsM) that enabled the rapid proliferation of various design and architectures of electrodes for the last three decades [86, 87]. NsM are materials that have at least one dimension in the nanometer range (typically between 1 and

100) nm [88] and display unique physical and chemical features due to the size effects. They provide a high specific surface area that enables enhanced loading of biochemical elements [89], excellent electron transfer promoting ability associated to the increased conductivity caused by the high fraction of atoms on the surface [90], enables control on morphology and high prospects for miniaturization to fabricate a compact and portable device.

Manipulation of the surface morphology or roughness enables to modify the physical and chemical behavior of the electrode surface. Borghi et al. [91, 92] showed that the roughness of the thin film electrode can be controlled to provide a high surface area that allows enhanced loading of protein that improves sensitivity. Another work from the same team showed that isoelectric point, wettability and pH of the electrode surface can be controlled by manipulating electrode surface roughness thereby to make the surface biocompatible [93]. The architecture of biomolecules immobilized on nanostructured surface is shown in Fig. 3.5.

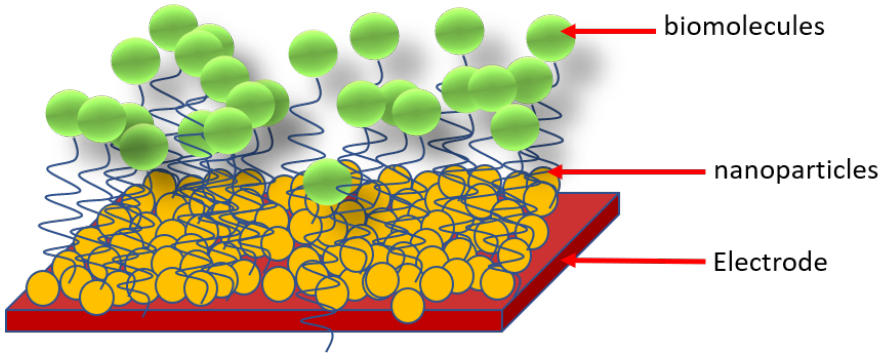

Figure 3.5: Nanomaterials modified electrode

A continuous effort has been produced to synthesize novel functional nanomaterials, deposition tools, and substrate material for building electrochemical sensors that satisfy the foregoing criteria [94, 95]. The conventional approaches employed for fabrication of nanostructured electrodes such as lithography and etching approaches that develop the desired nanostructure by removing materials starting from bulk by series of steps and it is well-established technology for fabrication of electrochemical sensors on the silicon wafer and glasses [96, 97]. However, they are impeded by physical and technical limitation, and the chemical used during etching is not suitable to apply on plastic substrates, an excellent candidate for manufacturing cost-effective, flexible and biocompatible sensors. In addition, the approaches are costly because of the cleanroom requirement, and very slow and multi-step process.

The direct fabrication methods such as atomic layer deposition, sol-gel nanofabrication, molecular self-assembly, vapor-phase deposition approaches produce nanostructured materials by stacking vaporized atoms, molecules or clusters layer by layer. The methods are widely used for producing electrochemical sensors on glasses, silicon, and composites [98, 99]. However, the desired metals should be heated to vapor at a higher temperature that may deform polymer substrates.

Electrochemical methods such as electroplating and electroless deposition approaches produce cost-effective conductive NsM with various surface features from solution, but they require prior metalization and activation of a

non-conducting substrate by reducing agents or a stabilizer respectively [100]. Screen and inkjet printing have been effectively used to fabricate several electrochemical sensors, however, high-temperature annealing limits the flexible substrate choice [101, 102]. On the other hand, SCBD technology is widely used for the fabrication of nanostructured electrodes with a tailored surface on the polymer substrate without deformation. The detailed description of the device is given in methods and materials. Moreover, the development of nanotechnology paved a way for the integration of electrochemical biosensors and microfluidic devices thus creating synergetic effect [31, 103].

3.2 Microlfuidics and biosensor on chip

Microfluidic technology provides a mechanism to control and manipulate a very small volume of fluids using channels with a dimension of tens to hundreds of micrometers [104]. Basically, microfluidics comprises of a channel for a flow of fluids, control and fluid delivery systems that manipulate the flow and provides a number of significant advantages. The emergence of microfluidics paved a way to miniaturization of the fluid system enabling portability and rendering new functionality and changing paradigm of experiments in chemistry, biology, medicine, and physical sciences [105, 106]. This system enables the integration of multiple processes like mixing, separation, detection, and labeling. Using microfluidic system laminar fluid flow can be achieved and allows to leverage physical, chemical and biological phenomena at lower dimensions applied to biosensors. Because the channel dimension is very small, the amount of reagents used are small, which can decreases costs and enables to do a complete experiment using small quantities of precious samples and reduced waste products. The reduced dimension also gives rise to faster diffusion, increased reaction time, reduced cost and portability [107].

3.2.1 Microfluidics fluid flow characteristics

Fluid flow in microfluidics is manipulated by pressure, magnetic, electric field and capillary fields. In pressure field flow, pumps(syringes pumps) are commonly used to drive fluid in the channel and creates velocity profile inside

the channel. In the case of electrokinetics, advection is induced by applying an electric field across the channel with charged walls to prompt the ions in the double layer move towards the electrode of opposite polarity, thereby creating motion of the fluid near the walls [108].

The characteristics of fluid flow through microfluidics systems is described by the Reynold number(R_e), the ratio between inertial force to viscous force [109] represented in equation 3.4.

$$R_e = \frac{\rho \nu D_h}{\mu} \tag{3.4}$$

where μ is the viscosity, D_h is the hydraulic diameter ρ is the fluid density and ν is the characteristic velocity of the fluid.

$R_e < 2300$ generally indicates a laminar flow and $R_e > 2300$ the flow is considered to be turbulent. In laminar flow molecules can be transported in a relatively predictable manner through microchannels and mass is transported through diffusion perpendicular to the flow direction. In addition Flows are linear and the flux line do not cross each other.

The mass transfer in microfluidic flow is measured by Peclet number(P_e) as shown in equation 3.5, which is the ratio of convective to diffusive mass transfer.

$$P_e = \frac{Uh}{D} \tag{3.5}$$

where U is flow velocity, h is length the microchannel and D s the species diffusivity

When $P_e << 1$ then diffusive effects dominate over convective transport,

and when $P_e >> 1$ the convective transport dominates the diffusive transport.

The fluid dynamics in microchannel with uniaxial incompressible flow at low R_e is governed by the Navier-Stokes equations(momentum conservation) given by equation 3.6.

$$\rho\frac{\partial U}{\partial t} = -\nabla P + \mu\nabla^2 U + \rho f \tag{3.6}$$

where μ is viscosity of the fluid, U is the velocity field along the channel, P is pressure, and f is the net force per unit volume acting on the fluid.

The laminar velocity profile for the flow in a microchannel with dimensions represented in the Fig. 3.6 obtained from equation 3.7. [110]

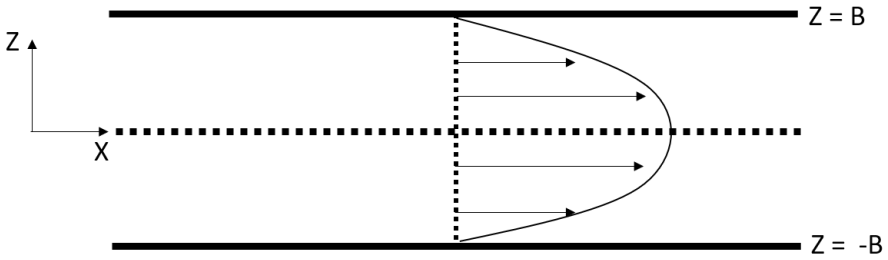

Figure 3.6: Schematic representation of the steady, fully developed laminar flow velocity profile in a rectangular channel of half-width B [111]

$$U_x = \frac{\Delta P B^2}{2\mu L}[1 - (\frac{z}{B})^2] \tag{3.7}$$

Here, ΔP is the pressure drop across the length L of the channel.

The average fluid velocity in the channel is described by equation 3.8.

$$U = \frac{1}{3}\frac{\Delta P B^2}{\mu L} \tag{3.8}$$

and the volumetric flow rate Q, which is the product of the above average velocity and cross-sectional area for flow 2BW given by the equation 3.9.

$$\frac{2}{3}\frac{\Delta P B^3 W}{\mu L} \tag{3.9}$$

3.2.2 Microfluidic biosensors on a chip

The integration of microfluidics and electrochemical biosensors give rise to a synergic effect that renders microfluidics LOC biosensors with enhanced performance, reduced cost, portability, and autonomy. In addition, the microfluidic system enables to introduce laminar flow induced convection onto confined electrode surfaces thus enhance the signal to noise ratio, sensitivity, a detection limit of electrochemical sensors and expand the scope of electrochemical biosensors application for autonomous flow investigation of online monitoring [156, 113, 29]. Because of these advantages, several attempts have been made to develop rapid prototyping methods for producing integrated microfluidic biosensor platforms using polymeric materials [114, 115, 116, 117]. Conventional microfabrication approaches which are adopted for polymer-based microfluidics rely on the use of expensive techniques (e.g. injection molding, casting, embossing) or time-consuming methods (e.g. laser writing, electron beam lithography) [57, 59]. Furthermore, a multistep production process for the assembly and sealing of the systems of different components after the electrodes fabrication (e.g. via adhesive or

thermal bonding) is required, and hence these strategies are inefficient for prototyping.

3.2.3 Rapid prototyping of integrated microlfuidic biosensors

Rapid prototyping involves executing three basic steps of additive manufacturing shown in Fig. 3.7. A 3D model of an object is created using computer-assisted designing(CAD) software. The model is then converted into Standard Triangulation Language (STL) format describing a polygonal representation of the part's surface geometry. Then slicer software is used to slice the 3D model into layers to generate gcode, commands to move parts within the printer [118]. The gcode is fed to the RP machine to print the physical model. Rp methods print materials from solid(FFF), liquid(stereolithography, SLA or polyjet) and powders(laser sintering, SLS).

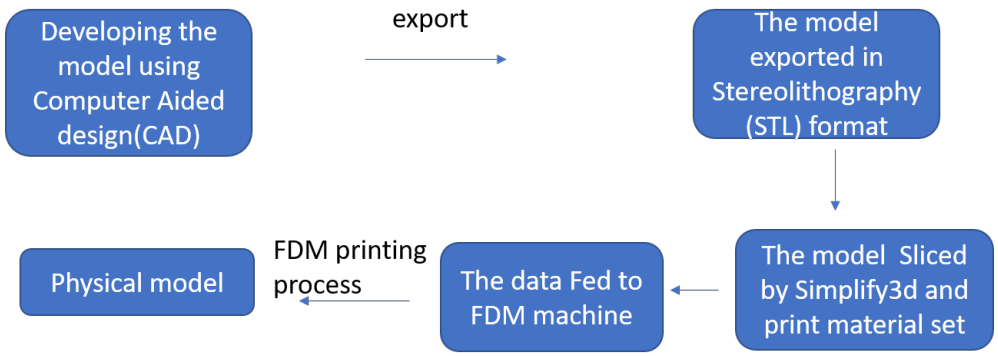

Figure 3.7: Basic steps of FFF operation

SLA builds a physical model by tracing ultraviolet laser beam or employing digital light processing to display the image of the 3D model onto the

surface of the resin-based photocurable liquid monomer and converting into a solid cross-section of the scale model layer by layer from the top to bottom or the reverse [121]. When the first layer is completed, the platform lowers by one layer thickness. To completely build the scale model, the liquid resin must be recovered atop the original layer and the process is iterated until the physical model is completed. The unpolymerized resin material is removed and the objected is consolidated by post-processing [122]. SLA was successfully employed to fabricate a microfluidic platform having high-resolution parts, very fine features, smooth surface, and relatively precise dimensions applied for microfluidic LOC electrochemical biosensors [123, 124, 125, 126]. However, most SLA base materials are propriety, and there are limited material choices. SLA printed objects are susceptible to dimensional as well as strength changes when they are continuously exposed to UV radiation. In addition, SLA is not versatile method to fabricate monolithically integrated microfluidics biosensors, due to the continuous coverage of the predecessor layers with resin to print the successive layer it is inconvenient to apply for manufacturing of monotonically electrode integrated microfluidics.

Polyjet 3D printer involves jetting drops of a thin layer of photopolymerizable liquid material onto the build plane and subsequently exposed to UV light to solidify the liquid, layer by layer [118]. The process is iterated until the complete model is obtained. Microfluidics devices printed using polyjet 3D printer showed faster build time, surface finish, multilateral print, and better dimensional accuracy [127, 20, 128]. Like SLA, polyjet printing is not convenient for fabrication of monolithically integrated microfluidics biosen-

sors because of the continuous jetting of the preprinted layers. And the printed objects are also prone to failures in UV environments.

In SLS case powder is used as base material to build a workpiece. During printing, a layer of powder is placed onto the print plate and then the infrared laser draws the structure solidifying powder into the solid material cross section, layer by layer. After the first layer is completed, another thin layer of powder is recoated on top of the original layer covering the whole area and exposed to a laser for solidification. When the print is completed, the object is recovered from powder and thoroughly cleaned to remove powder residues. Because of the difficulty of removing powders from enclosing, SLS is not widely used for the fabrication of microfluidic devices. Moreover, because the base material is prepared in powder form, the technology is limited by material choice [129].

FFF process employs filament melt extrusion to build a physical model. The FFF head is resistively heated to melt thermoplastic filament and the melt is subsequently extruded through the nozzles [130]. The nozzle is numerically controlled to move in x, y and z-direction to make object cross-sections while laying melts on a print bed layer by layer that solidifies and eventually forms the object. Once the first layer modifies, the next layers are superimposed and the process continues until the object piece is ready. Unlike SLA, FFF allows creation of functional component integration window because it employs thermoplastics filament melts to additively manufacture the workpiece by localized material deposition [131] creating controlled printing of

the complementary enclosing top layer on the preprinted layer, and has been already proven to be convenient for fabrication of microfluidic devices such as reliable and robust reactors, and electrochemical biosensors with integrated wires, nanoparticles, glass slides and electrodes [132, 133, 134, 135].

FFF printed devices can be used without postprocessing so that functional components can be directly embedded into the microfluidic platform during printing offering an extra benefit to speed up the scale-up manufacturing of the integrated microfluidic biosensors [136]. In addition, FFF requires low maintenance cost, the printed object maintain dimensional integrity at various environmental conditions, no toxic materials are released, raw materials are inexpensive and there is a broad range of production grade thermoplastics available to make custom-based materials choice [137, 138, 139]. Recently, Gowers SA and his colleagues developed FFF printed microfluidics that integrates clinical microdialysis probes and needle type biosensors and which can be used for continuous monitoring of human tissue metabolite levels[140]. Liver cancer cells biosensor was developed by Damiati et. al by integrating commercial electrodes into FFF printed structure [145]. Ludmila K. and his team have developed Sensitive, and specific microfluidics integrated biosensor combining FFF printed microfluidics platform and used for detection of influenza hemagglutinin [146]. Glassy carbon electrode was combined with FFF printed microfluidics platform for lab-on-a-chip detection of nucleic bases [147]. 3D-Printed fluidic devices for nanoparticle preparation and flow-injection amperometry using integrated prussian blue nanoparticle-modified electrodes was developed by Bishop G. et.al [148]. However, in

the reported integrated biosensors assembly externally prepared, or commercially obtained electrodes were integrated into microfluidics using a modular like approach. Therefore, in order to exploit such versatile FFF technology for manufacturing of monetarily electrode integrated microfluidic biosensors, novel electrode fabrication technologies that can produce strongly anchored electrodes with FFF base materials, and a novel fabrication technique that bridge the combination are vital. The SCBD technology was proposed to fills this gap. The detailed discussion of SCBD is presented in following chapter.

Chapter 4

Methods and Materials

4.1 Working and counter Electrode fabrication

4.1.1 Supersonic Cluster Beam Deposition

Supersonic cluster beam deposition(SCBD) is a family bottom-up approach, which deposits nanostructured materials from cluster source. The SCBD is performed in a chamber maintained at room temperature so that fabrication of nanostructured transducers on different polymer substrates with low glass transition temperature is possible. In addition, the SCBD technology enables the production of large area thin films with a tailored roughness and porosity [73, 149, 150]. The schematics of the apparatus is shown in Fig. 4.1. The cluster source PMCS comprises of a ceramic box with holes for introducing the pulse of inert gases using a solenoid valve and nozzle that connects with vacuum expansion chamber that contains cascades of aerodynamic lenses.

The expansion chamber is connected to the high vacuum deposition chamber through the skimmer.

The operation principle of the SCBD technology is based on execution of three primary steps, first cluster generation in the gas phase, second cluster beam extraction, selection and collimation by supersonic expansion and the third is deposition of the desired nanostructures by spraying the cluster beam over a substrate [72].

The cluster generation mechanism in the first chamber, PMCS is shown in Fig. 4.2. One side of the ceramic cavity was connected to a solenoid valve for introducing pulses of inert gas, and the desired metallic rod was hosted through a channel.

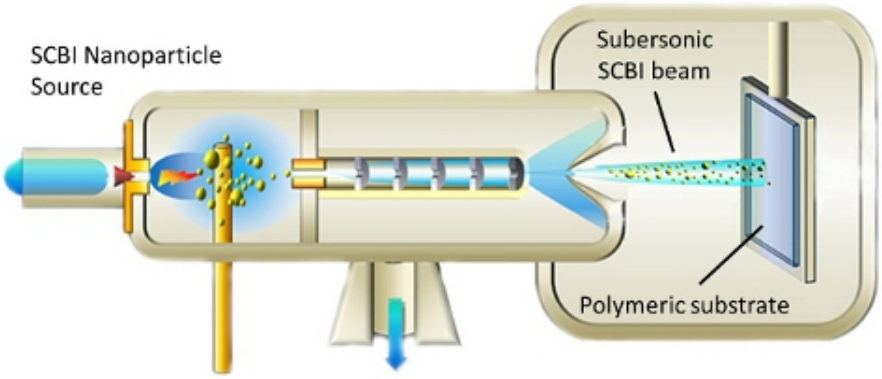

Figure 4.1: Schematic representation of the SCBD apparatus[72]

The metallic target was connected to high cathodic potential with respect to anode placed inside the cavity. Pulses of inert gases usually (He or Ar) delivered into the ceramic box by solenoid valve.

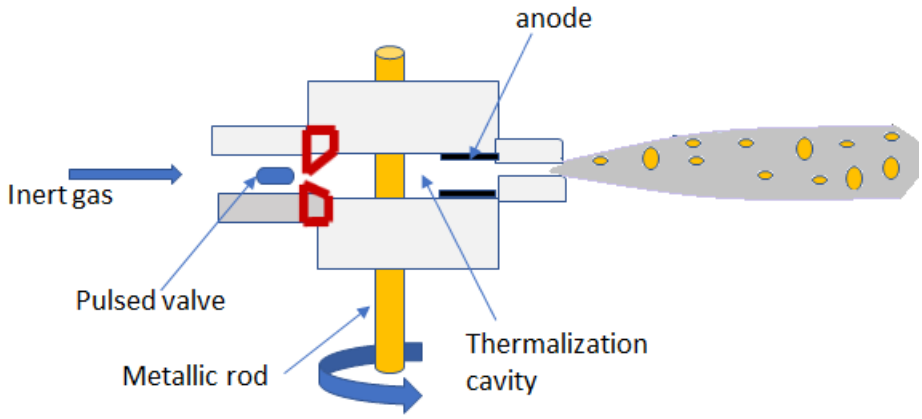

Figure 4.2: PMCS, cluster generation [71]

When the solenoid valve is opened for introduction of inert gas, large pressure difference created inside cavity induce the formation of supersonic gas jet directed to the target [71]. This gas jet forms confined plasma jet that vaporizes the rode into atoms by sputtering. The vaporized atoms collide and thermalize with the carrier gas forming clusters of various size. Uniform ablation is achieved by rotating the rod. Due to the high-pressure difference between the cluster source and expansion chamber, the mixture of clusters and carrier gas expand supersonically through the small nozzle forming seeded supersonic beams.

The beam enters the chamber that contains aerodynamic lenses with series of openings. These lenses supported with supersonic expansions select and collimate the beam as shown in Fig. 4.3. During supersonic expansion, bigger particles are separated from the beam line and deposited on the walls of the lenses due to bigger inertia, while smaller particles stay in the beam

line and get collimated through every supersonics expansion after each lens. The supersonically expanded and aerodynamically collimated beams render high deposition rate. [150, 151, 152]

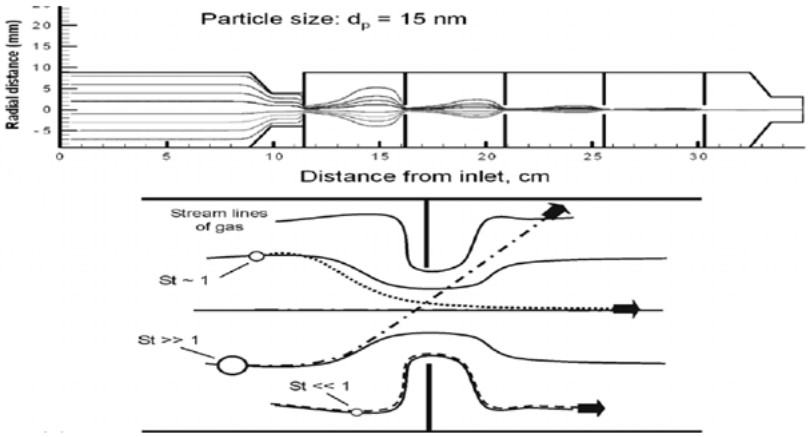

Figure 4.3: Basic principle of aerodynamic size-selection and focusing

After a series of such events collimated intense beam passed through the skimmer and intercepted by a substrate for deposition. The substrate attached to the stage in the high vacuum deposition chamber moves vertically and horizontally enabling large area deposition by spraying on the substrate. The metallic nanoparticles are implanted into the plastic matrix thereby rendering strongly anchored metallic thin films. Besides room temperature deposition, the energy of clusters is adjusted to be below the cohesive energy of the matrix so that no chemical reaction occurs on the substrates. The cluster beam flux is monitored in real time by a quartz microbalance placed close to the substrate. The SCBD technology combines, pulsed microplasma cluster source, aerodynamic collimation, and supersonic expansion and near room temperature deposition provides the capacity to deposit large

area nanostructured materials on temperature sensitive materials such as thermoplastic materials, common base materials for FFF technology.

4.1.2 Experimental

Nanostructured Au thin film working, and counter electrodes were fabricated by directly depositing gas phase clusters on FFF printed ABS substrate employing SCBD tool equipped with a Pulsed Microplasma Cluster Source (PMCS). Au metallic rod was placed in a ceramic cavity the cluster was generated. The Au cluster-carrier gas mixture expands into an expansion vacuum chamber (at a pressure of about 10^{-5}) forming a seeded supersonic beam and subsequently collimated using a set of aerodynamic lenses. The Au cluster beams are accelerated by the supersonic expansion towards the ABS substrate mounted in the high vacuum chamber (10^{-7}) with a kinetic energy of approximately 0.5 eV/atom to penetrate the FFF printed ABS substrate surface through a mask thereby forming ABS-metal nanocomposite layer. By monitoring the deposition rate through quartz microbalance 250 nm thick nanostructured conducting Au thin films were obtained.

4.2 Reference electrode fabrication

4.2.1 Electrodeposition

Electrodeposition(ED) is a versatile and low-cost deposition method used to fabricate Ag/AgCl reference electrode on conducting surface from solution.

The ED system consists of electricity, a plating bath, and complementary electrodes shown in Fig. 4.4 The plating bath prepared such that it contains ions of the metal to be deposited, an electrolyte for better conduction and adhesion promoters. The deposition happens by passing electricity while both the metal to be deposited(anode) and the substrate(cathode) are immersed in a plating bath. Then, Constant current(galvanic) or Voltage(potentiostatic) to pump electrons into the cathode where deposition occurs. This electron transfers to metal ions in the solution and reduces onto the electrode to be deposited. The reduced metallic ions are constantly replenished by the anode(clean plate or wire), the depositing metal, which is dissolved into the solution in the form of the metal ions. The thickness of the deposited material is controlled by deposition time, the amount of current or voltage and deposition rate, and the amount of deposited material is calculated using Faraday's law, equation 4.1. [153]

$$W = \frac{It\mu}{nF} \tag{4.1}$$

Where W – weight of the deposited material; μ – weight of one mole of the metal; n - number of electrons transferred F – Faraday's constant, F = 96485 Coulombs.

4.2.2 Experimental

Microfluidics integrable Ag/AgCl thin film quasi-reference electrode was fabricated on FFF printed ABS substrate by selective electroplating using cluster assembled Au strip as a conduction path. In this case capability of

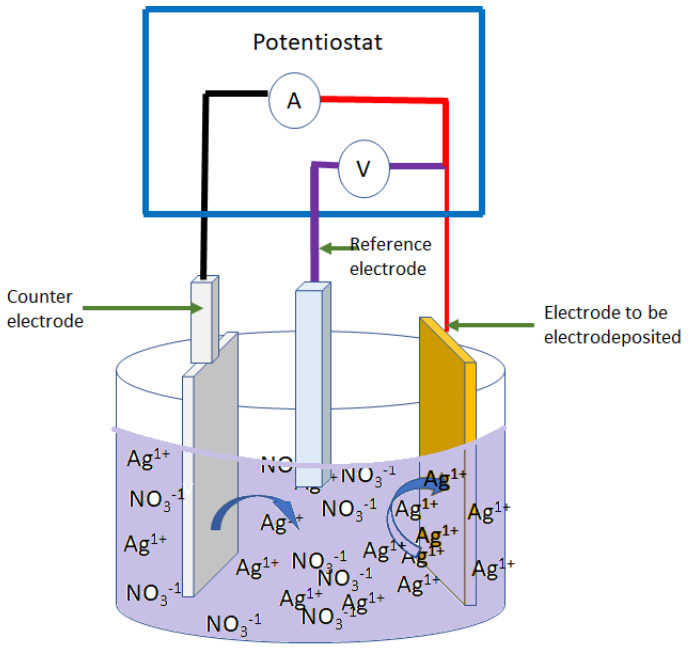

Figure 4.4: A simple electrochemical plating system

the SCBD metallization of plastic materials was exploited for manufacturing functional reference electrodes on FFF printed ABS thermoplastic material. Accordingly, the ABS substrate was metalized by deposition of Au metallic clusters, which was later used as a conduction path for performing electroplating. And fresh Ag plating bath was prepared by strictly following recipe of the Tel Aviv University team. After metallization, Ag electroplating was performed in the chronopotentiometry setup using the metalized ABS substrate as cathode and Ag plate (purity: 99.9% Good fellow) as the anode and applying uniform current density of 15 mA-cm^{-2} for 15 minutes while the solution was continuously stirred using a magnetic stirrer. The amount of applied current and deposition time was adopted from the electroplating

protocol provided by the Tel Aviv University electrochemistry team led by professor Yosi. After Ag thin film was successfully electroplated, the film was cleaned with deionized water to remove plating bath residues and blow dried by nitrogen stream. Subsequently, the electroplated thin film connected to the anode and Pt mesh (purity: 99.9% Good fellow) connected to cathode terminals on the potentiostat and dipped into 0.1M HCl aqueous solution for anodization. The current density of 5mA-cm^{-2} was applied for 15 minutes for chlorination of 25-30% Ag to formal layer. Proper deposition of both Ag and AgCl layers were assessed based on the trends of the curve displayed during electroplating. The fabricated electrode was characterized by performing stability duration test by measuring open circuit potential against the commercial/AgCl(3.5M, KCl, from GAMRY) in 0.01M KCl solution with time. In addition, its potential functionality as the quasi-reference electrode was tested by employing it as a reference electrode in the three-electrode electrochemical cell to perform cyclic voltammetry of Ferro/Ferricyanide redox couple.

4.3 Microfluidics device fabrication

4.3.1 Fused Filament Fabrication

Fused Filament Fabrication Rapid Prototyping is one of the most economical additive manufacturing technologies that use a thermoplastic filament to produce end-use physical model directly from virtual data. The fabrication process starts by developing a virtual model using CAD. Then the model was extracted in the stereolithography format. The model was sliced into layers by pertinent slicing software to generate, the machine code that calculates the printing path, speed, and other functions during actual printing. The values of operational parameters such as layer height, %infill, print speed, melt temperature are set at this stage. Then, the data was downloaded into SD card and fed into the FFF machine to print the physical model. During printing as shown in Fig. 4.5, ABS filament unwound from the spool mounted on top of the printer was fed into the extrusion head, which was heated to 230^{o}C.

The nozzle heats the plastic to a temperature just above its melting point using resistive heaters and it was numerically controlled to move in the x, y, and z-direction to fabricate an object cross-section while laying melts on a print bed. Then, the semi-liquid melts were extruded through the nozzle and deposited onto a build platform, cools and solidify immediately. After the first layer was completed the head raises by next layer thickness set up during slicing and the extrusion nozzle prints the next layer additively layer

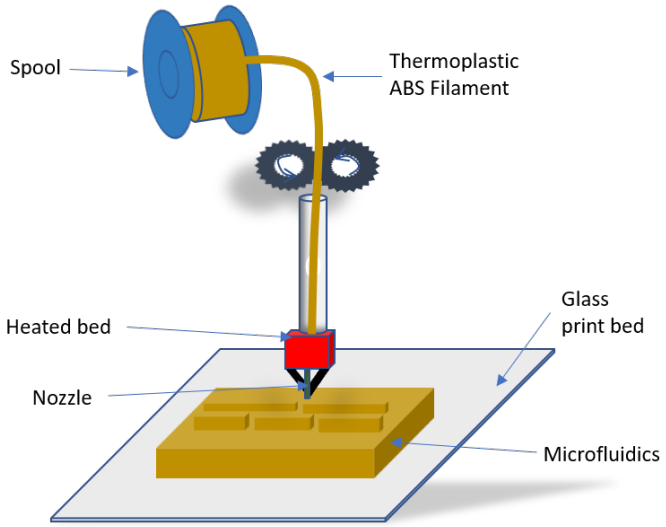

Figure 4.5: Schematic representation of FFF operation

by layer until the scale model was completed.

4.3.2 Experimental

Delta WASP 2040 fused deposition modeling(FFF) printer, with a nozzle diameter of 0.4 mm, and the heated bed was employed to fabricate the microfluidic platform of the electrode integrated microfluidics sensor. It is a consumer grade printer with a closed chamber that maintains uniform temperature during fabrication. The printer has a glass bed with the print area of 200 mm x 200 mm. To print the physical model, the fundamental steps of rapid prototyping showed in Fig. 3.7 was employed. Production-grade transparent ABS material (ORIB-TECH Germany) was used as a base material.

For this work the microfluidic platform was fabricated in two steps: the

bottom part with an open channel and three canals were printed first. Then, the top layer was printed by offsetting the nozzle distance by the thickness of the bottom layer from the print bed. In this case, the nozzle starts from the surface of the bottom layer, completing the microfluidics device. All operational parameters of the printer such as layer height, temperature, print speed, and infill were thoroughly investigated to obtain an optimum print condition to print the smoother or uniform surface.

4.4 Device design and fabrication strategy

In the proposed design of the three-electrodes integrated electrochemical sensor, electrodes were monolithically integrated into the microfluidic platform shown in Fig. 4.6. The model was created using inventor Autodesk 3D designing free software. The electrochemical unit consists of 3 mm x 4 mm Au thin film working the electrode, 1 mm x 3 mm Ag/AgCl thin film quasi-reference electrode, and 3 mm x 5 mm Au thin film counter electrodes, all of them deposited in the channel. These electrodes are connected to circular connection pads through 2 mm wide and 7 mm long metallic extension. The microfluidic platform consists of 33 mm x 27 mm planar bottom substrate that contains 23 mm x 3 mm x 3 mm channel, three 2 mm x 7mm x 3 mm canals that protects metallic films extension, which connect electrodes with the connection pads, and 33 mm x 17 mm planar top layer, which incorporates two holes with 4 mm diameter used to fit commercial connectors that join the integrated microfluidics sensor with an external syringe pump.

To realize the device, a two-step fabrication process shown in Fig. 4.7 was

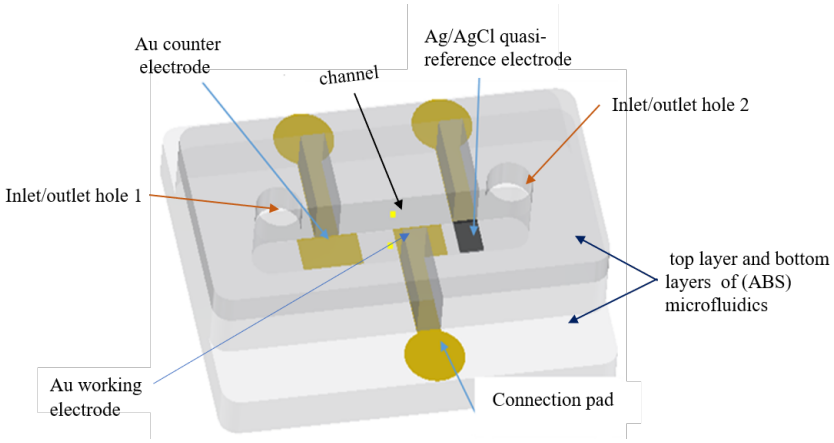

Figure 4.6: Design of the proposed electrode embedded electrochemical microfluidic biosensors device

considered as the feasible method to embed SCBD electrodes into the FFF printed microfluidics. The method was based on the process of printing, interrupting and resuming at any suitable stage to create electrode integration window. Thus, this requires printing the bottom layer prior to the top layer, interrupting to embed electrode and resuming printing to fabricate the top layer to complete the device. In the first phase of the work, a customized two-step FFF microfluidics fabrication strategy with SCBD deposited electrode integration steps was developed. The strategy was to print the bottom layer having an open channel and canals first, and subsequently, the print was stopped. Then the three electrodes were deposited. To protect the metallic thin films that extended through the canals over which the print nozzle traces while overprinting the top layer, we developed a passivation method using acetoxy silicon adhesives. The three canals were filled with acetoxy silicon

until it levels with the canal well and dried at room temperature. After 20-30 minutes, the passivated substrate was transferred to FFF print bed and the top layer was overprinted enclosing the channel, thereby completing the device. With such a fabrication method, we able to combine SCBD, FFF and the existing fabrication methods for rapid prototyping of the electrode integrated microfluidics electrochemical sensors.

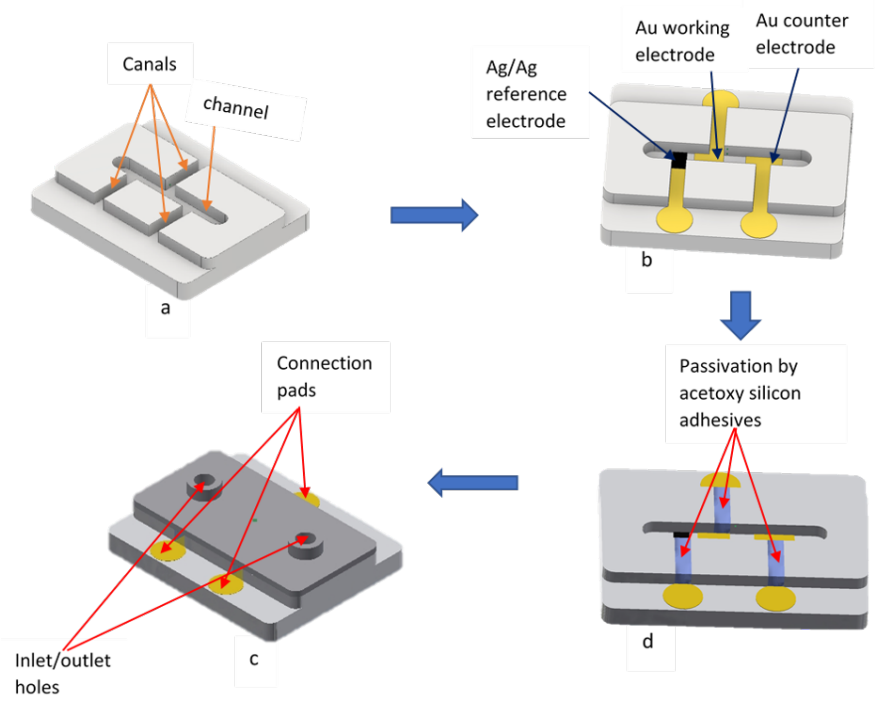

Figure 4.7: The proposed fabrication strategy

4.5 Surface smoothening by acetone vapor

FFF printed materials exhibit a significant surface roughness resulting from poor surface finish attributed to the inherent layer by layer manufacturing mechanism employed. Thus, the canals and channel of the microfluidic system were smoothened using acetone vapor to reduce the potential influence of the surface roughness on electrochemical properties of the electrodes. The acetone vapor was chosen because ABS material melts in acetone. The smoothening was performed by executing the steps shown in Fig. 4.8. The glass jar wall was totally covered by tissue papers and cold acetone was poured on it so that it can later produce uniform vapor can be produced. After the FFF printed ABS bottom layer fitted with PLA mask was placed on the lid, the glass jar was sealed upside down. The mask was used for selective exposure of only the channel and canals so that essential feature on the bottom layer was preserved from acetone attack.

The smoothening was monitored by measuring the roughness profile with a stylus profilometry with respect to time. Prior to acetone treatment FFF printing parameters (speed, layer height, temperature, printing orientation, and infill percentage) were optimized to acquire the surface with roughness profile less than the maximum vertical range of the profilometer (130 μm). The roughness of FFF printed the surface with layer height greater than 0.15 mm usually gets out of the vertical rage of a profilometer. Consequently, it is difficult the get complete roughness profile.

Figure 4.8: Surface smoothening by treating with cold acetone

4.6 Electrode passivation

Passivation was employed to protect the electrodes from damage during overprinting the top layer to enclose the channel. In the proposed fabrication strategy metallic extensions were buried inside the canal walls so that they can be protected from damages that would be induced by the printer nozzle traces during overprinting the top layer as shown in Fig. 4.7b. The canals must be filled up in order to render the sealed channel without side leaks and facilitate smooth overprinting process as depicted in Fig. 4.7c. Acetoxy silicone sealant material was proposed to be applied for sealing the canal openings. Acetoxy silicone sealant is commonly used in electronics for passivation of electrical connectors on the circuit board because of its neutrality with metallic connections and a very good tendency to adhere to various substrates. It also cures relatively rapidly, developing skin within 10 minutes and completely cures within 20 to 30 minutes at room temperature. Moreover,

it is thermally insulating, cost-effective and faster-curing adhesive. Using acetoxy silicone sealant the canals were filled up to complete sealing of the canals by over-printing. This approach paved a convenient way for completing the device by overprinting of the top layer, facilitating the integration of the FFF and SCBD technologies for the desired purpose.

4.7 Fabrication strategy of the integrated microlfuidic biosensors

The device was designed in such a way that SCBD deposited three electrodes based electrochemical cell unitarily integrated into FFF printed microfluidic platform so that the analyte detection was eventually performed in the channel. To realize this device, the two-step manufacturing technique incorporating electrode integration step was proposed. For fabrication of electrodes with the desired dimensions, three masks containing the dimension of working, counter and reference electrode geometry, and a sample holder, which accommodates two samples at a time was produced by the workshop at the physics department of the University of Milan. Each mask contains only the design of one type of electrode so that it could fit our two step-fabrication protocols.

The proposed complete prototyping strategy is schematically shown in 4.9. In the first part of the procedure, the bottom layer containing the fluidic channel and three passivation canals was printed using Delta WASP 2040. Greases and print residues were removed by washing with soap and

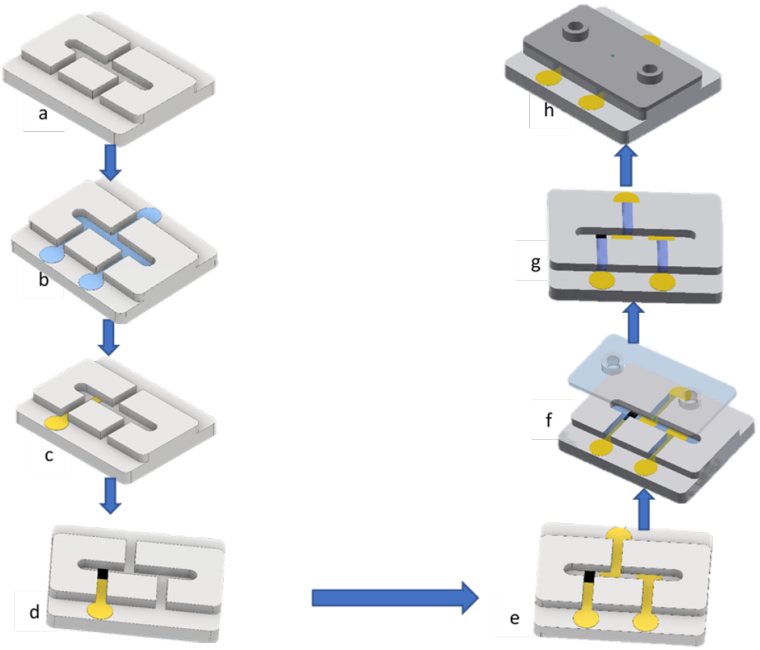

Figure 4.9: Schematic representation of electrode integration strategy for manufacturing of the integrated microfluidics electrochemical sensor. The bottom layer a, acetone smoothening b, metalization c, Ag/AgCl fabrication d, working and counter electrode deposition e, silicon passivation f, over-printing the top layer g, The prototype device h

water, sonicating in ethanol for 30 minutes and rinsing with deionized water. In the next step, the channel and canals were smoothened by treating with cold acetone vapor for 1 hour. Then, the substrate was thoroughly washed with soap and water, sonicated in ethanol and rinsed with deionized water. Then, the reference electrode region was selectively metalized by depositing the Au strip using SCBD through the mask containing the reference electrode geometry. Ag/AgCl quasi-reference electrode was selectively electroplated in the channel using the metalized region as a conduction path for current. Thereafter, the mask containing working and counter electrode

geometry was fitted to the sample holder and mounted to SCBD chamber for deposition of the Au thin film working and counting electrode. After the three electrodes were successfully produced, the canals were passivated by filling with acetoxy silicone sealant and dried at room temperature. While the silicon sealant was curing rectangular open box with the dimension of 33 mm x 27 mm x 3 mm was FFF printed. Subsequently, the bottom layer with the passivation elements was fitted in this open box. The open box was employed to support the sample on the print board during overprinting the top layer. Then, the top layer containing two holes was overprinted to seal the channel completing the device.

4.8 Electrochemical characterization methods

Electrodeposition and electrochemical characterization were performed using Reference 600+, a high-performance, research-grade potentiostate/galvanostat, ZRA(Gamry potentiostat). And Au disc, Pt wire and Ag/AgCl(3.5M, NaCl) electrodes purchased from BASi were used as complementary electrodeposition and electrochemical characterization were performed using Reference 600+, a high-performance, research-grade potentiostat/galvanostat, ZRA(Gamry potentiostat). And Au disc, Pt wire and Ag/AgCl(3.5M, NaCl) electrodes purchased from BASi were used as complementary electrodes to characterize the SCBD fabricated electrodes. For all electrochemical characterizations performed in this work, analytic grade potassium ferricyanide $K_3Fe(CN)_6$ and Potassium ferrocyanide($K_4Fe(CN)_6$) redox couples purchased from Sigma

Aldrich were used as the electrochemical probe. Also, analytic grade KCl and KNO_3 obtained from Sigma Aldrich were used as the electrolyte in $K_3Fe(CN)_6$ and $K_4Fe(CN)_6$ solution. For all electrochemical characterizations performed in this work, analytic grade potassium ferricyanide $K_3Fe(CN)_6$ and Potassium ferrocyanide($K_4Fe(CN)_6$) redox couples purchased from Sigma Aldrich were used as the electrochemical probe. Also, analytic grade KCl and KNO_3 obtained from Sigma Aldrich were used as the electrolyte in $K_3Fe(CN)_6$ and $K_4Fe(CN)_6$ solution.

Electrochemical characterization of the SCBD manufactured electrodes and prototype device performed using linear cyclic, Electrochemical Impedance spectroscopy. The electrodes were investigated in stagnant solutions in a beaker in conjunction with complementary commercial electrodes in conjunction with commercial electrodes from BASi in 10mM $[Fe(CN)_6]^{3-}/[Fe(CN)_6]^{4-}$ probe in KCl/KNO_3 electrolyte. Both cyclic voltammetry and chronoamperometry used in this work are based on the following concepts. When potential is applied in the way that electron transfer from the electrode to the solution it produces reduction current.

$$Fe(CN)_6]^{3-} + e^- -> [Fe(CN)_6]^{4-} \tag{4.2}$$

When the opposite potential is applied in the way that electron transfer from solution to electrode it produces oxidation current.

$$[Fe(CN)_6]^{4-} -> Fe(CN)_6]^{3-} + e^- \tag{4.3}$$

The prototype device was studied in both stagnant and flowing $K_3Fe(CN)_6$ and $K_4Fe(CN)_6$ solution in KCl/KNO_3 electrolyte. The stagnant solution based characterization was conducted pumping in the solution until it fills up the channel. Then, the desired electrochemical characterization was performed. After every complete set of characterization, the device was rinsed with de-ionized water.

Flow dynamic electrochemical characterization was introduced using Kd Scientific 100 syringe pump connected to the prototype device through a tube joined to commercial connectors which was fitted to the inlet/outlets of the integrated system. The solution pumped in through the inlet hole flow passed through the surface of integrated electrodes and pumped out through the outlet holes. Then cyclic voltammetry was performed while the solution was flowing past the electrode surface. The flow rate and scan rate were varied as desired to assess the potential application of the device for online monitoring.

4.8.1 Cyclic Voltammetry

Cyclic Voltammetry, electrochemical techniques widely employed to measure the concentration of an analyte by measuring electric current related to oxidation and reduction of electroactive species by applying potential [154]. Among several families of voltammetry techniques, cyclic voltammetry is the simplest and widely used method to investigate interfacial characteristics of an electrochemical cell.

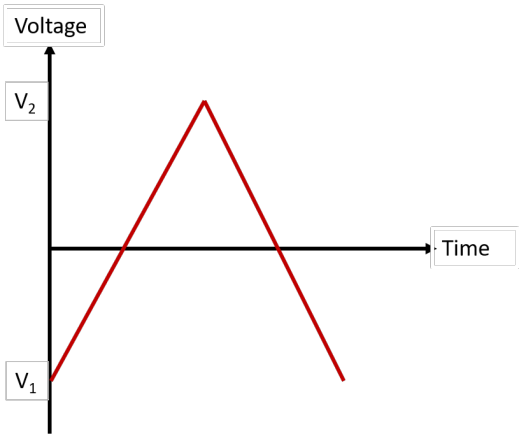

Figure 4.10: Excitation potential

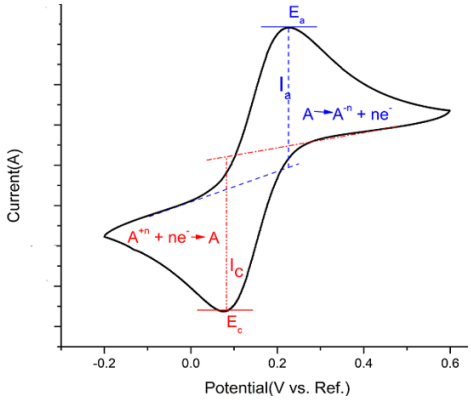

Figure 4.11: The voltammogram

In this case, the potential of the working electrode is swept at a fixed rate (in volts/second) between V_2 and V_1, and the generated current is recorded with respect to time giving a voltage-current curve. Performing the CV for the stagnant solution containing a redox couple at different scan rates, electrochemical reversibility, and electron transfer rate are acquired to assess the performance of electrode materials. For reversible reaction the peak-to-peak separation (Ea-Ec) is equal to 59/n mV (at 295 K) and the positions of peak voltage remains the same as a function of voltage scan rate, the ratio of the peak currents is equal to one, and the peak currents are proportional to the square root of the scan rate given by equation 4.4.

$$I_p = 2.69n10^5AC(\frac{nF\nu D}{RT})^{\frac{1}{2}} \tag{4.4}$$

where n is number of transferred electrons, the ratio of oxidation peak current(I_a) to reduction peak current (I_c) give 1.

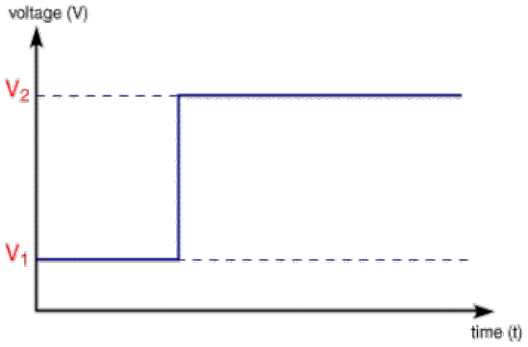

Figure 4.12: Excitation potential for chronoamperometry

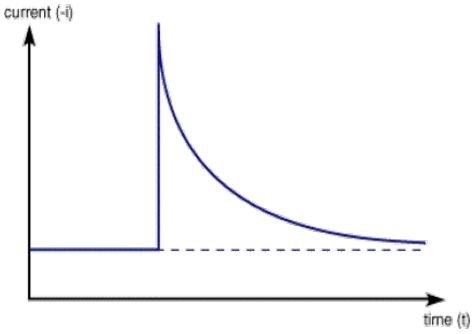

Figure 4.13: Typical chronoamperometry response

4.8.2 Chronoamperometry

Amperometric methods measure the current resulting from the oxidation/reduction of electroactive species on the working electrode by applying a constant potential. Usually, a three electrode electrochemical cell is employed, where current is measured between the working and counter electrode while the potential is applied between the working and the reference electrodes. The method has an advantage of high selectivity, good detection limits, lowcost and good reproducibility [155]. Chronoamperometry measures diffusion controlled current as a function of time by applying potential step that varies from a value at which no Faradic reaction occurs to a potential at which the concentration is totally consumed. The current flow with time is described by the Cottrell equation 4.5. This technique has a good signal to noise ratio and employed to investigate the active surface area, diffusion coefficient, and concentration [141].

$$It = \frac{nFACD^{\frac{1}{2}}}{\pi^{\frac{1}{2}} t^{\frac{1}{2}}} \tag{4.5}$$

4.8.3 Electrochemical Impedance spectroscopy

Electrochemical Impedance Spectroscopy(EIS) is a powerful tool to investigate impedance of an electrochemical cell to flow of current. The impedance data provides quantitative information about the interface phenomena of the developed electrochemical cell such as diffusion, electron transfer rate, adsorption mechanisms, charge transfer resistance, the capacitance of EDL and surface features electrodes [142]. It also provides quantitative characteristic information about the electrodes, an electrochemical species, and biochemical elements. By selecting pertinent equivalent circuit models of the electrochemical interface phenomena, qualitative and quantitative information can be extracted about the resistors, capacitors, and inductors that represent different sources of impedance in the electrochemical cell.

EIS measures the impedance of an electrochemical system by applying a small amplitude of an alternating signal to the electrochemical cell. The ideal electrochemical interface is assumed as a combination of resistance, capacitance, and inductance. Resistors represent the resistance to the charge-transfer process at the electrode surface(R_p), and uncompensated or electrolyte resistance R_c, the resistance of electrolyte to ion transport. Capacitors are associated with the electrochemical double layer, and inductors are associated with adsorption/desorption processes at an electrode surface. For

nonideal electrochemical interface double layer capacitor is represented by constant phase element (CPE) while the Warburg element(Z_W) is used to represent the diffusion or mass transport impedances of the cell at low frequency.

EIS responses of electrochemical cells are usually represented in Nyquist and Bode. Nyquist plot represents real and imaginary impedances in a complex plane and used to evaluate electrode polarization resistance, electrolytic solution resistance, and double layer capacitance. The explicit frequency-dependence of the impedance of the electrochemical system is depicted in the Bode plot. In this case, impedance is plotted against frequency that explicitly shows the effect of the spectrum on the impedance and phase drift so that values of equivalent circuit elements can be obtained from the maximum points of phase shift.

4.9 Flow electrochemical characterization

Flow dyamic electrochemical detection approach is employed for analysis of an analyte in a flowing solution. The solution is enabled to flow passed electrode surface while the electrochemical measurement is performed. Among several. This methods increase current and hence the sensitivity of an electrochemical biosensor by introducing additional mass transfer by convection. Among several forced convection introduction mechanisms, in channel flows, where the volume flow rate (v) controls the convection to the surface are built integrating the electrochemical unit into a microfluidics platform.

4.9.1 In channel flow voltammetry

In channel flow cell cyclic voltammetry sensor was developed by incorporating electrochemical sensors into the rectangular channel. The flow was introduced using syringe pumps that enables control of convection rate as shown in Fig. 4.14. The channel design and flow rates are adjusted so that the flow pattern on the electrode surface is laminar. For the stagnant

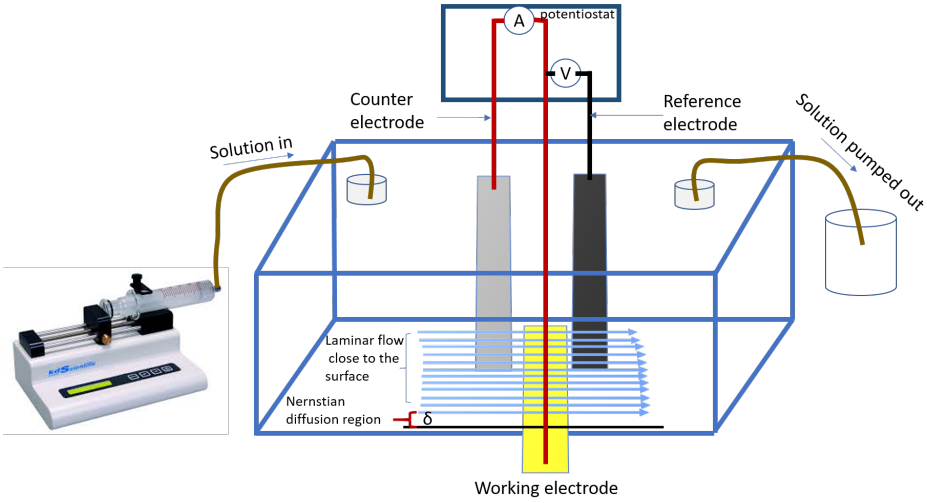

Figure 4.14: In channel flow analysis

solution, diffusion is the dominant means of mass transfer to the electrode surface, which occurs when the concentration gradient is created between the electrode surface and the bulk solution. The diffusion thickness expands to the bulk with time. Inflow analysis, fresh analytes are supplied to the electrode surface through forced convection besides the diffusion. The channel dimension and flow rates are adjusted for the flow pattern on the electrode are laminar. In this case, the thin liquid layers slide on one another parallel

to the electrode surface and the fluid layer near to the electrode surface is stationary.

The Stationary layer, Nernst layer exhibits the concentration variation with respect to distance from the electrode surface. Because convection supplies fresh analyte the diffusion layer remains constant and the diffusion is limited to this region.

Therefore, the sensitivity of electrochemical biosensors can be improved by predictably controlling the channel dimension and convection rate.

For reversible electrochemical reaction the electron transfer property in a channel with a rectangular cross-section is predicted by the Levich model [143] represented in equation 4.6.

$$I_L = 0.244nFD^{\frac{2}{3}}wC(\frac{Vx^2}{dh^2})^{\frac{1}{3}} \tag{4.6}$$

Where, h, x, h and w are constants for the cell size and V is the volume flow rate.

4.10 Optimization of roughness of FFF printed ABS surface

The surfaces roughness of FFF printed ABS substrate was investigated by printing substrates with varying process parameters such as layer thickness, slicer, and speed that play an essential role on FFF printed material surface quality. Basically, the largest surface roughness contribution stems from

the seam formed by bonding two adjacent filaments due to the inherent layer by layer manufacturing process implemented in additive manufacturing. This can be clearly observed from optical microscope images of substrates printed with the layer height of 0.06 mm, the smallest layer height that can be achieved by the commercial grade DLTA WASP FFF used in this research, 0.08 mm, 0.1 mm, 0.2 mm and 0.25 mm, the maximum layer thickness achieved by the same printer are shown in Fig. 4.15. It can be observed as the layer thickness varied the samples exhibited contrasting surface features such as zigzag seams, uneven surface with microcracks, and periodic coarser and thicker seams across the print direction. The samples printed with the lower layer thickness (samples a and b) showed relatively uniform surface profiles because the extruded roads are very thin that the bonding between the adjacent roads created shorter and thinner seams. On the other hand, the samples printed with the higher layer thickness (samples d and e) exhibited surfaces with thicker and coarse roads. The possible reason for this observation is that the width of the road becomes thicker with increasing the layer height so that it created larger and thicker seams during bonding with the preprinted adjacent layers which then caused the formation of clearly visible hills and valleys.

The effect of print speed on the ABS surface finish was investigated by printing test samples at different speeds but at the same lower layer thickness. Because of the relatively lower surface roughness obtained for the samples printed with lower layer height, 0.06 mm layer height was used in this study. Fig. 4.16 shows the optical microscope images of test samples printed at 50

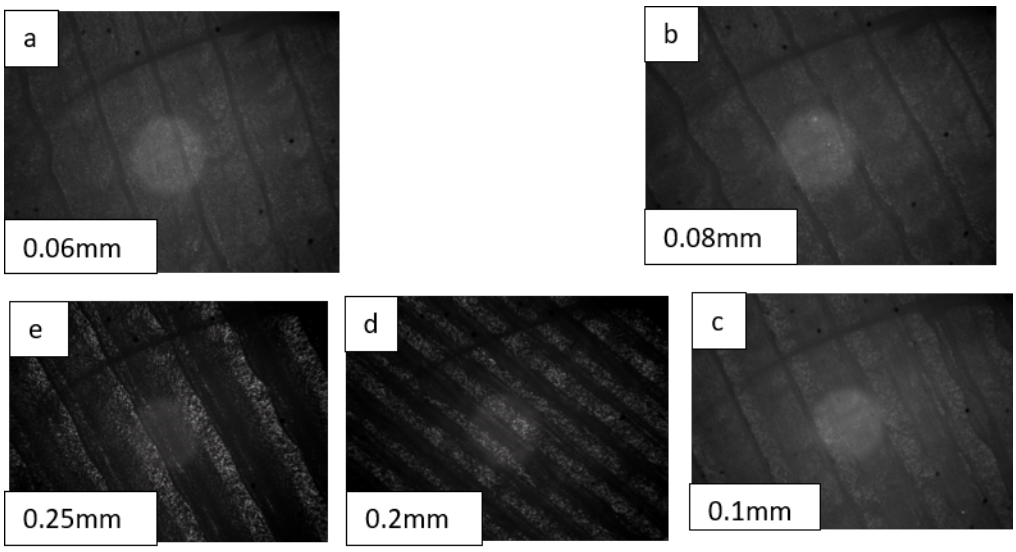

Figure 4.15: Optical microscopy image of FFF printed ABS surfaces printed with different layer height

$\frac{mm}{s}$ and 100 $\frac{mm}{s}$ with the layer thickness of 0.006 mm. The samples printed at slower speed exhibited thinner, and non-straight seem, while those samples printed at faster speed showed thicker and coarser seams. The samples printed with different layer height exhibited diverse surface profiles. The effect of commonly used slicer software on the surface roughness is shown in Fig. 4.17. For both slicers, the R_q and $R_z$values increased as the layer thickness increased. The samples sliced by cura and printed with low layer height showed smaller values for the samples sliced by cura as compared to those sliced at lower layer height, and the reverse was obtained for the higher layer height. The minimum R_q values obtained was greater than 20 μm, which is greater than the conventional thickness of electrodes used to build electrochemical sensors, which is between 0.2 and 0.3 μm. Therefore,

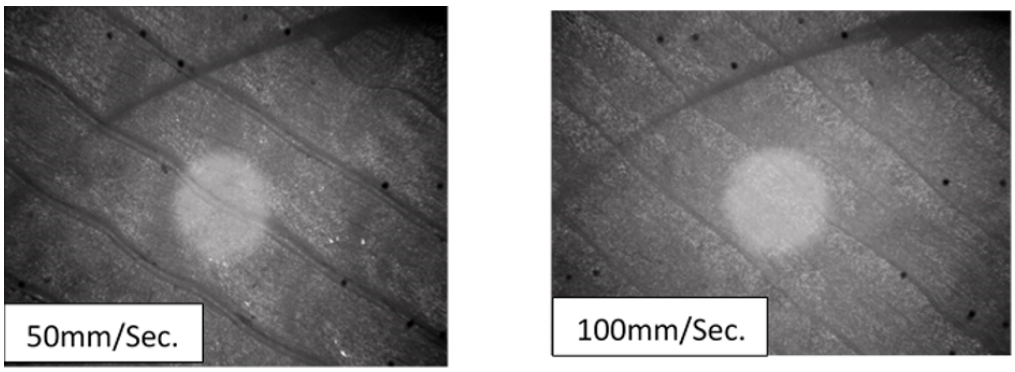

Figure 4.16: Optical microscopy of FFF printed ABS surfaces printed with slower and faster print speed

to mitigate concomitant negative effects on the functionality of sensors it is vital to reduce the roughness of FFF surface. By that method, FFF technology can be employed for manufacturing of electrode integrated microfluidics electrochemical sensors.

4.11 Smoothening of FFF printed ABS surface

Fig. 4.18 shows the bottom layer of the prototype before and after the acetone treatment. The untreated substrates showed uneven surface features with visible print lines. However, when the channel and canals were selectively exposed to cold acetone vapor in a sealed glass jar they became smooth and shiny as shown in Fig. 4.18B. This is because the acetone vapor melts away the uneven surface features and the melt forms bond with the adjacent layer thereby forming a smooth surface. In a well-sealed container, one hour

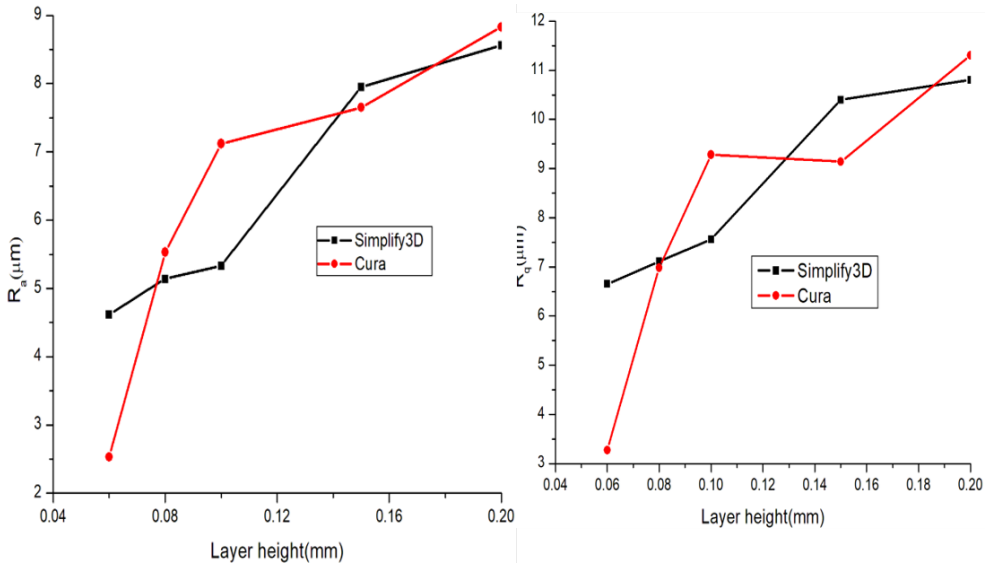

Figure 4.17: FFF printed ABS surface roughness profile for cura and simplify3D

cold acetone vapor exposure is sufficient to smoothen out the uneven surface features. However, prolonged exposure could cause structural damage as shown in Fig. 4.19. The over-exposed samples were mechanically frail, and the canals were distorted. The reduced mechanical strength impeded overprinting of the top layer to seal the channel. The difference in average roughness values between the untreated and acetone vapor treated sample surfaces is clearly visible on the graph shown in Fig. 4.19. After the samples were treated with cold acetone vapor surface roughness was considerably reduced. The R_a value obtained by optimizing only process parameters was 3.694 μm. Then, it was reduced to 2.281 nm after treating with acetone.

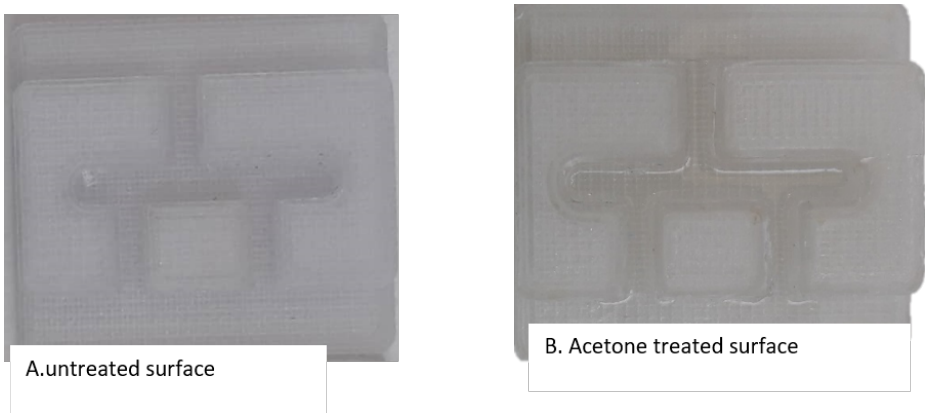

Figure 4.18: Bottom layer of the before and after acetone exposure

Figure 4.19: Bottom layer after prolonged exposure to acetone vapor

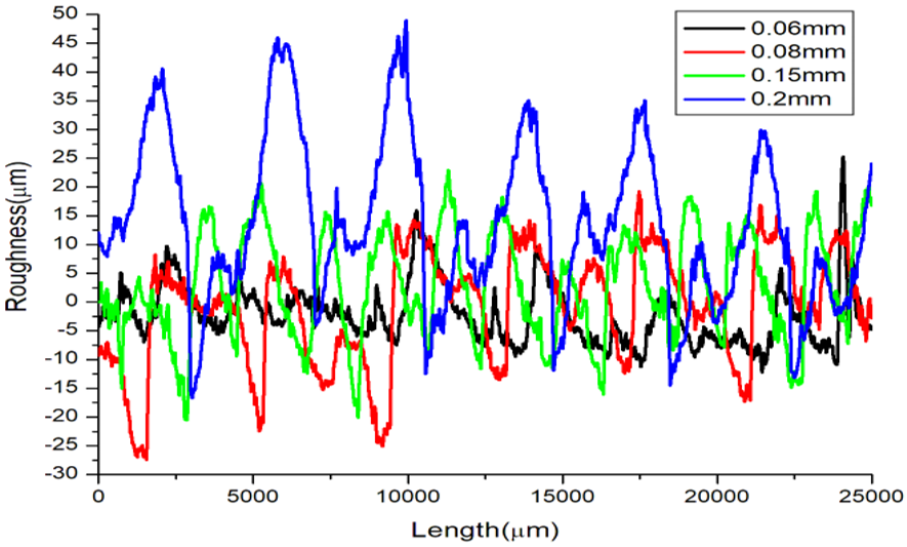

Figure 4.20: Roughness profile of FFF printed ABS surface measured by profilometer

4.12 Fabrication and characterization of monolithic microfluidics with enclosed channel

The monolithic microfluidics platform with a sealed channel fabricated by the two-step process using FFF is shown in 4.21. The device consisted of analyte inlet and outlet holes, and a sealed channel. The liquid leakage test performed by pumping yellow and red dyes into the channel showed that

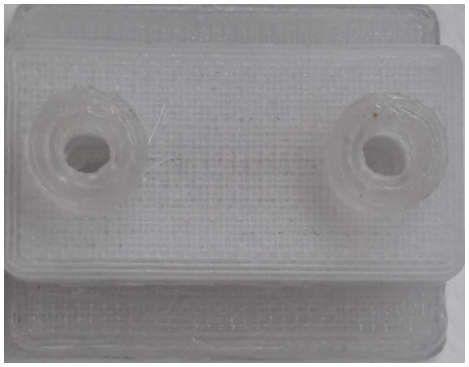

Figure 4.21: Monolithic microfluidics platform printed by two step

the liquid delivered by the inlet hole flowed passed through the channel and emerged through a tube fitted to the outlet hole as shown in Fig. 4.22. The test indicated that the liquid dyes were constrained only in the channel implying that the channel was leak free.

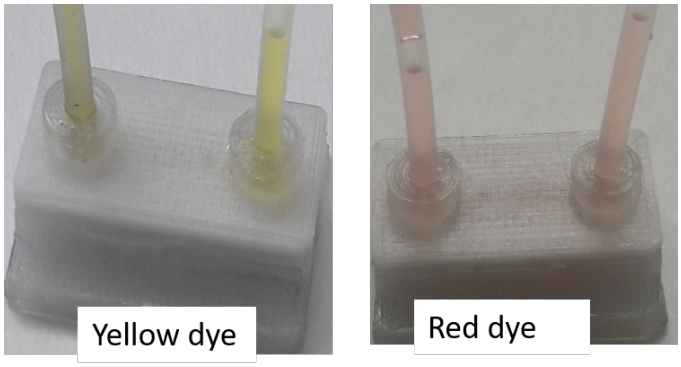

Figure 4.22: Leakage test performed pumping yellow and red dyes

4.13 Prototyping of integrated electrochemical microlfuidic biosensors

The prototype was manufactured by integrating cluster assembled Au working and counter electrodes, and Ag/AgCl quasi-reference electrode into FFF printed microfluidics platform executing the step-by-step integration scheme shown in Fig. 4.23. The cluster assembled Au strip was employed to metalize the reference electrode region on FFF printed ABS bottom layer of the prototype as shown in Fig. 4.23a. The shiny white layer is shown in Fig. 4.23b was obtained by selective electroplating of the Au strip in Ag plating bath by applying constant current density of 15 mA-Cm^{-2} for 15 minutes. Anodization of the Ag layer in 0.1 M HCl aqueous solution by applying constant current density of 5 mA-Cm^{-2} for 15 minutes resulted in dark brown Ag/AgCl layer as shown in Fig. 4.23c. Then, the cluster assembled Au work-

ing and counter electrodes were deposited through the mask containing their respective shape and dimensions, Fig. 4.23d. And the canals were filled with acetoxy silicone sealant and dried at room temperature for 30 minutes, Fig. 4.23e. The prototype with the integrated electrodes and enclosed channel shown in Fig. 4.23f was obtained by overprinting the top layer.

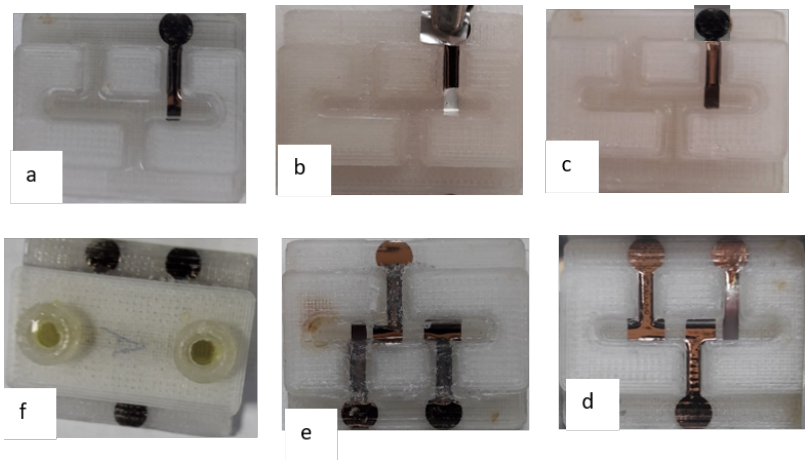

Figure 4.23: Prototyping of electrode integrated electrochemical microfluidics biosensors platform

The electrical test performed before and after the integration showed no change in the electrical properties of the electrodes. The electrical test performed using a multimeter by the setup shown in Fig. 4.24 before and after the overprinting the top layer after passivating the canals with the acetoxy silicon sealant didn't show the difference.

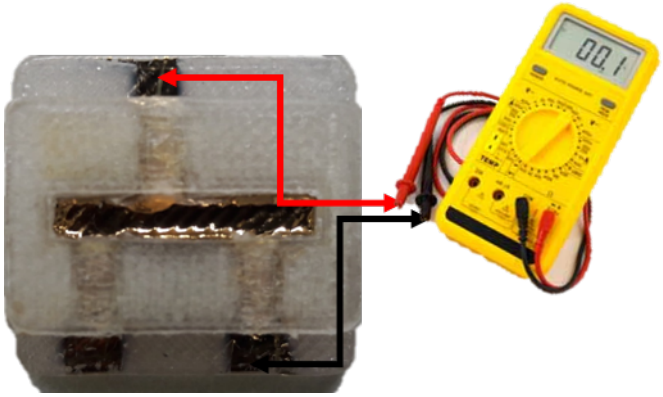

Figure 4.24: Electrical Test

4.13.1 Liquid leakage test

When red and yellow dyes were perfused into the channel at various flow rates using a syringe pump, there were no side leaks observed. In addition, there was no air bubbles observed when the dyes were perfused at varying flow rates while the prototype was submerged in water, Fig. 4.25. Therefore, it can be concluded that the dyes were only enclosed into the channel implying that the channels were properly enclosed and sealed by overprinting the top layer.

Figure 4.25: Liquid leakage test

Chapter 5

Results and discussion

5.1 Electrochemical characterization

In this chapter, electrochemical performance of Au thin film working and Ag/AgCl quasi-refrence electrodes were assessed by performing cyclic voltammetry in 10 mM ferro/ferricyanide. The prototype of microfluidics integrated biosensors platform was employed for detection and analysis of Ferro/Ferricyanide redox couple in stagnating mood using cyclic voltammetry, chronoamperometry, and EIS. The potential application of the integrated device for flow analysis application was investigated using flowing ferro/ferricyanide solution and performing cyclic voltammetry.

5.1.1 Characterization of Ag/AgCl quasi-reference electrode

Ag/AgCl quasi-reference electrodes were electroplated on the FFF printed ABS substrate after ABS was metalized using cluster assembled Au strip as shown in Fig. 5.1. Highly conductive 250 nm Au strip fabricated by the SCBD was employed as a conduction path for selective electroplating of Ag film on ABS substrate. Fig. 5.1A shows the white shiny Ag layer manufactured by electroplating Ag atop the Au strip for 15 minutes. The uniform and complete coverage of the Ag layer on Au strip was achieved by the presence of a large active surface area attributed to the cluster assembled surfaces that were used as active nucleation center during electroplating. The manufactured Ag film remained adhered to the Au stripe during resining with water and blow drying with nitrogen, post-processing process needed to remove plating bath residue, implying that the Ag film strongly adhered to the Au strip.

Fig. 5.1B displays the dark brown AgCl layer grown by anodization of the

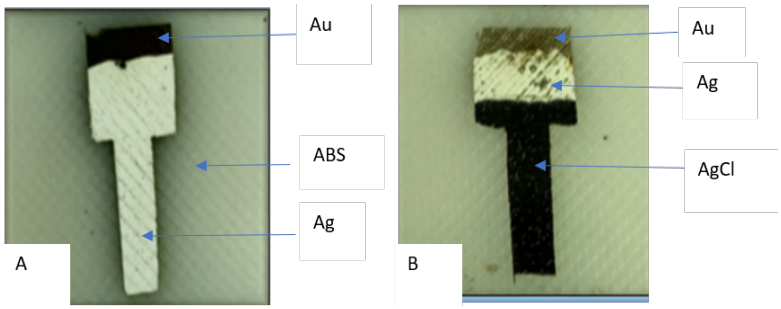

Figure 5.1: Electroplated Ag/AgCl quasi-reference electrode

Ag film in 0.1 M HCl solution under 5 mA-cm^{-3} constant current density for 15 minutes. During this process 25-30% of the Ag film was converted to the AgCl layer by applying one-third of the current density used for plating Ag

layer. The manufactured Ag/AgCl as well showed a strong adhesion to the Ag layer during the post-cleaning process.

The reference electrode stability throughout the entire electrochemical mea-

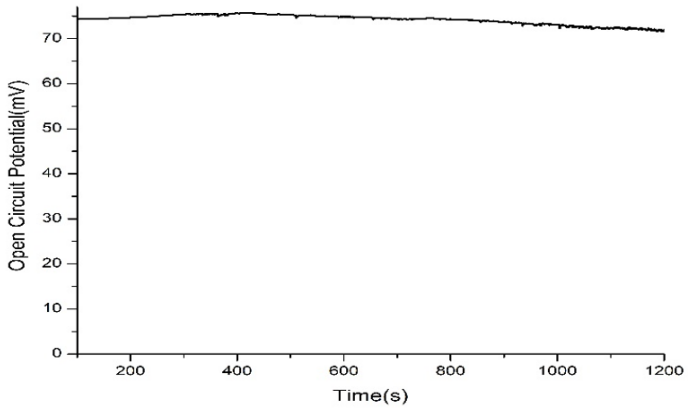

Figure 5.2: Ag/AgCl stability with respect to commercial Ag/AgCl (3.5M, KCl) in 0.1 M KCl solution

surement was essential because a stable reference electrode provides a constant reference potential with which the potential of the working electrode is measured. The stability test was performed by measuring the evolution of open circuit potential difference between the newly fabricated electrode and the commercial Ag/AgCl(3.5 M, KCl) in 0.1 M aqueous solution of KCl.

The measurement showed that the newly prepared electrode exhibited a good stability for up to approximately 1000 seconds before displaying 1 mV potential drift as shown in Fig. 5.2. This stability duration is adequate for the common electrochemical sensor to perform the complete measurement.

The electrochemical functionality of the manufactured Ag/AgCl film was

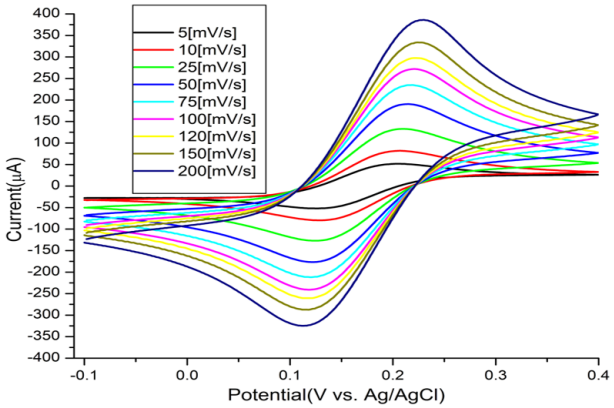

Figure 5.3: Current-voltage curve of 10 mM ferro/ferricyanide in 0.1 KCl

investigated by employing it as quasi-reference electrode in the three-electrodes electrochemical cell in conjunction with commercial Pt counter and Au working electrodes to measure the voltammogram of 10 mM $[Fe(CN)_6]^{3-}$ /$[Fe(CN)_6]^{4-}$ in 0.1 MKCl. In Fig. 5.3 it can be seen that the current-voltage curve displayed oxidation and reduction faradaic current with the oxidation and reduction potentials of the probe. In Fig. 5.4 the limiting current increased with the scan rate and the ratio of oxidation peak current to reduce peak current is almost equal to 1 implying that the chemical reaction was diffusion dependent and reversible. Accordingly, it can be concluded that the manufactured Ag/AgCl film can function as a quasi-reference electrode in a three-electrode electrochemical cell. In addition, the successful fabrication of Ag/AgCl layer on SCDB metalized ABS substrate implies that the SCBD can be employed as technology to combine the prevailing electrochemical fabrication methods with 3D printing technology.

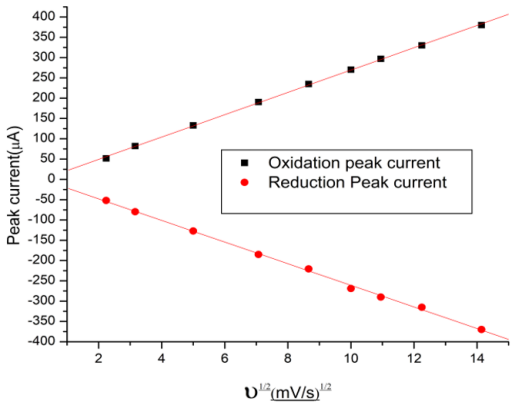

Figure 5.4: Oxidation and Reduction peak current of 10 mM ferro/ferricyanide in 0.1 KCl

5.1.2 Characterization of cluster assembled Au thin film working electrodes

Optical microscope image of Au cluster assembled thin film electrode fabricated on FFF printed ABS substrate using PMCS is shown in Fig. 5.5. Au thin film with thickness of 250 nm and resistance of 7 Ω was successfully deposited on cold acetone vapor smoothened ABS substrate.

The thin film electrode was characterized in cyclic voltammetry characterization setup in 10 mM $[Fe(CN)_6]^{3-}/[Fe(CN)_6]^{4-}$ probe performed using the cluster assembled Au thin film as working electrode in three-electrodes electrochemical unit in conjunction with Pt and Ag/AgCl(3.5M, KCl) electrodes. Current- voltage curve obtained by scanning between 0.6 and 0 V is shown in Fig. 5.6. The curve clearly shows oxidation and reduction peaks of the probe with the Faradic peak oxidation and reduction currents. The

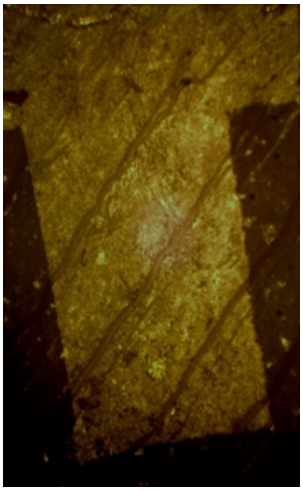

Figure 5.5: Optical microscope image of Au cluster assembled thin film

peak currents increased with the increase of scan rate without a pronounced shift in peak position implies that the electrochemical reaction occurred on the surface of the Au thin film electrode was reversible. The ratio of oxidation and reduction current was approximately 1, and the peak oxidation and reduction current fitted linearly with square root of the scan rate, with R^2 = 0.999 as seen in ig. 5.7, which confirms the diffusion dependent reversible reaction. The minimum peak to peak potential separation obtained was 74.0 m$\frac{V}{s}$n at the scan rate of 10 m$\frac{V}{s}$, as shown in the table 5.1.

Theoretically the peak-to-peak separation is 59 n and independent of scan rate. The deviation between the experimental and theoretical values are attributed to uncompensated resistance that depends on the concentration of electrolytes. Therefore, the Au cluster assembled thin films deposited on FFF printed ABS substrate possess huge potential to function as a working electrode in a three-electrode electrochemical sensor.

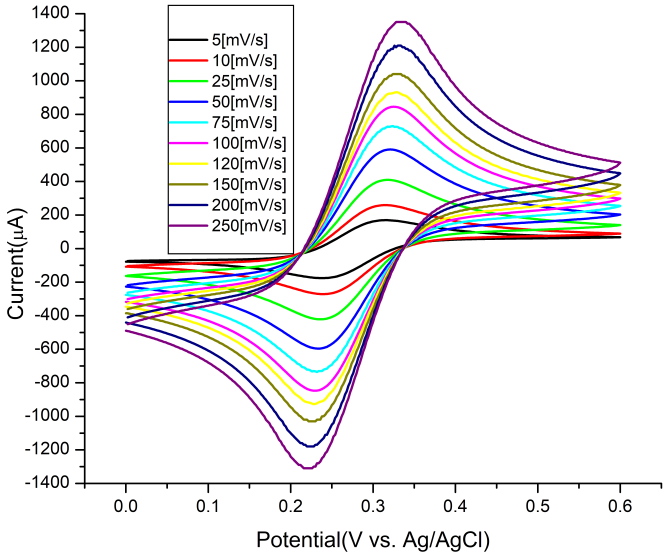

Figure 5.6: Current-voltage curve of 10 mM $[Fe(CN)_6]^{3-}/[Fe(CN)_6]^{4-}$ in 0.1 M KCl

Table 5.1: Oxidation and reduction potential, and peak-to-peak separation of Ferro/Ferricyanide

Scan rate(mv)	Ea(mV)	Ec(mV)	δE(mV)
5	316	176.2	78
10	314	240	74
25	318	236.1	81.9
50	320	234.1	85.9
75	328	226.1	102
100	326	230.1	95.9
120	328	228.1	99.8
150	332	224.1	108
200	330	224.1	106
250	332	220.1	112

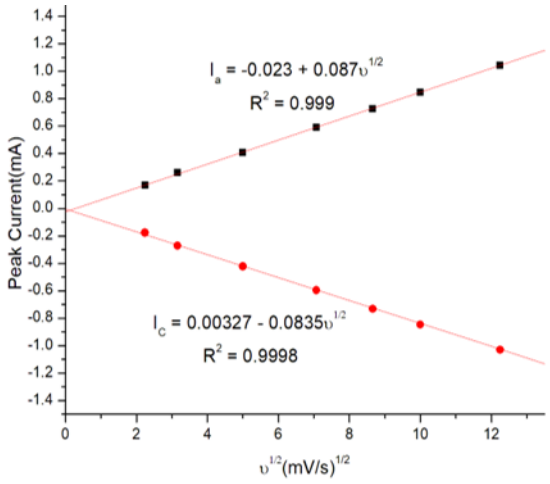

Figure 5.7: Peak oxidation and reduction current

5.1.3 Cyclic voltammetry of Ferro/Ferricyanide using the prototype of electrode embedded electrochemical microfluidic sensor

Fig. 5.8 shows cyclic voltammogram of 10 mM $[Fe(CN)_6]^{3-}/[Fe(CN)_6]^{4-}$ in 0.1 M KCl stagnant solution obtained using the prototype for different can rate, and scanned between 0.4 and -0.4 V. The curve shows two clear oxidation and reduction peaks attributed to the $[Fe(CN)_6]^{3-}/[Fe(CN)_6]^{4-}$. With the increase of scan rate the oxidation and reduction peak currents of the probe increased. Also, the ratio of the oxidation peak current to reduction peak current was approximately 1, and the curve linearly fitted with $R_2 = 0.999$(oxidation) and 0.998(reduction) as shown in Fig. 5.9, which are the characteristics of diffusion dependent reversible electrochemical reaction. However, the oxidation peak positions shifted the right while the reduction peak position shifted to the right when the scan rate increased. The minimum peak−to−peak separation obtained for lower scan rate was 110 mV and significantly increased when the scan rate was increased deviating from the theoretical value of 59 mV. Therefore the electrochemical reaction of $[Fe(CN)_6]^{3-}/[Fe(CN)_6]^{4-}$ occurred on the Au working electrode can be considered as quasi-reversible. The pronounced deviation of the peak−to−peak potential from theoretical value and its dependency on the scan rate may be attributed to the instability of cluster-assembled Au working and counter electrodes. During the electrochemical measurement, we observed instantaneous and rapid attack happening on Au working and counter electrodes as they were placed in $[Fe(CN)_6]^{3-}/[Fe(CN)_6]^{4-}$ solution containing KCl elec-

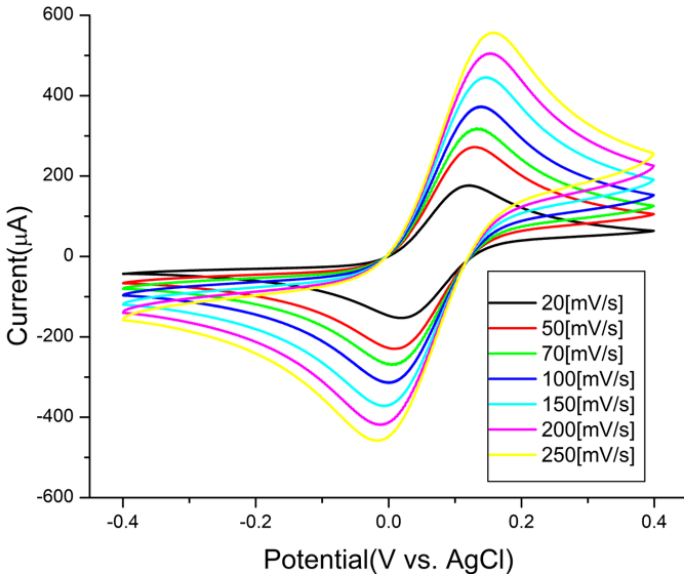

Figure 5.8: Current-voltage curve of 10 mM $[Fe(CN)_6]^{3-/4-}$ in 0.1 M KCl solution obtained using the prototype

trolyte. This was possibly by the fact that cluster assembled Au electrodes are highly susceptible to chlorine attack because the similar attack was not observed when the electrochemical measurement was performed using the same probe in the 1 M KNO_3 electrolyte. After running 100 cyclic voltammetry in 10 mM $[Fe(CN)_6]^{3-}/[Fe(CN)_6]^{4-}$ in 1 M KNO_3 electrolyte no drift or shift in potential was not observed as shown in Fig. 5.10. Therefore, KNO_3 electrolyte was used for further electrochemical characterization of the prototype.

Cyclic voltammogram of 10 mM $[Fe(CN)_6]^{3-}/[Fe(CN)_6]^{4-}$ recorded using newly manufactured electrode incorporated microfluidics electrochemical sensor is shown in Fig. 5.11 In this case, oxidation and reduction

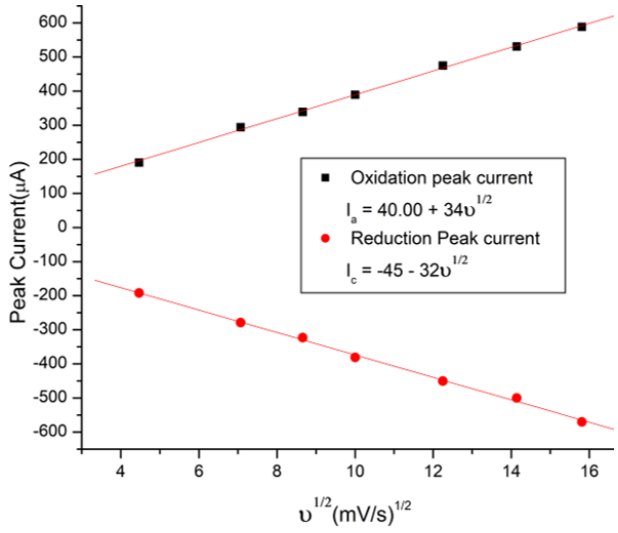

Figure 5.9: Peak anodic and cathodic currents of 10 mM $[Fe(CN)_6]^{3-/4-}$

peak currents of $[Fe(CN)_6]^{3-}/[Fe(CN)_6]^{4-}$ increased when the scan rate increased. shown in Fig. 5.11, peak-to-peak separation was reduced to 81 mV for the scan rate of 25 mV, and the separation did not show significant variation when the scan rate was increased. The ratio of anodic to cathodic peak currents was approximately 1 and the curve linearly fitted(R^2= 0.998) indicating diffusion dependent reversible electrochemical reaction of the $[Fe(CN)_6]^{3-}/[Fe(CN)_6]^{4-}$occurred on the cluster assembled Au working electrode.

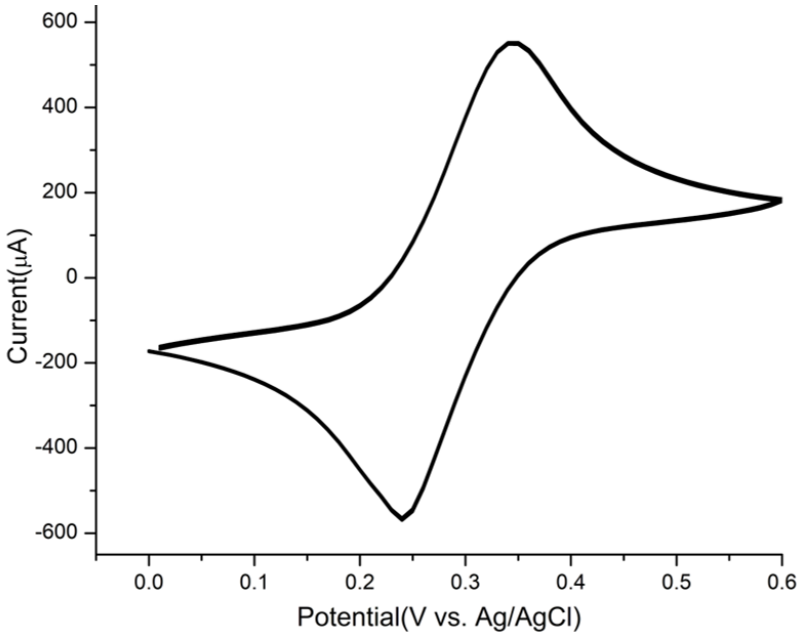

Figure 5.10: 100 cycles cyclic voltammograms recorded at 50 mV/s in 10 mM $[Fe(CN)_6]^{3-/4-}$ in 1 M KNO_3

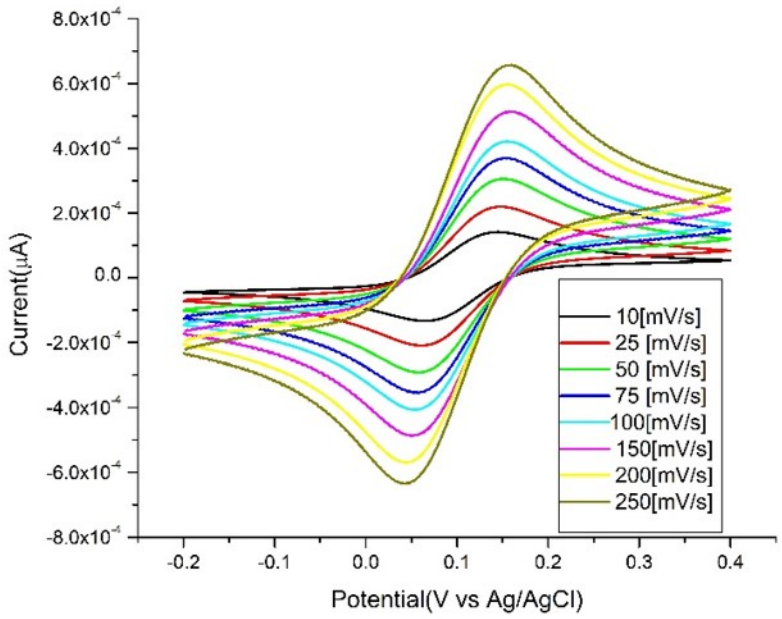

Figure 5.11: Cyclic voltammograms recorded using the prototype in 10 mM ferro/ferricyanide in 1 M KNO_3

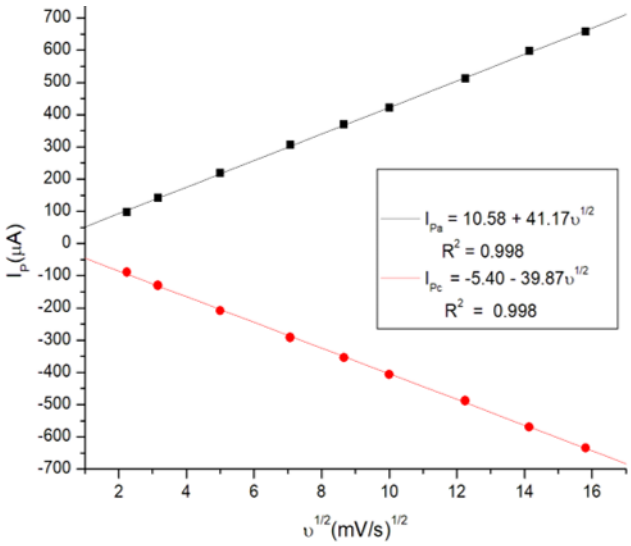

Figure 5.12: Anodic and cathodic peak currents for 10 mM ferro/ferricyanide in 1M KNO_3

5.1.4 Chronoamperometry of Ferro/Ferricyanide using the prototype of electrode embedded electrochemical microfluidic sensor

Fig. 5.13 shows typical chronoamperometric curves obtained for different concentration of $[Fe(CN)6]^{3-}$/ $[Fe(CN)_6]^{4-}$ using the prototype of electrode integrated microfluidic biosensor. As clearly seen faradaic currents were produced by apparent oxidation of $[Fe(CN)_6]^{3-}$/$[Fe(CN)_6]^{4-}$ redox couple on the surface of the incorporated working layer into the bulk solution, which sub-

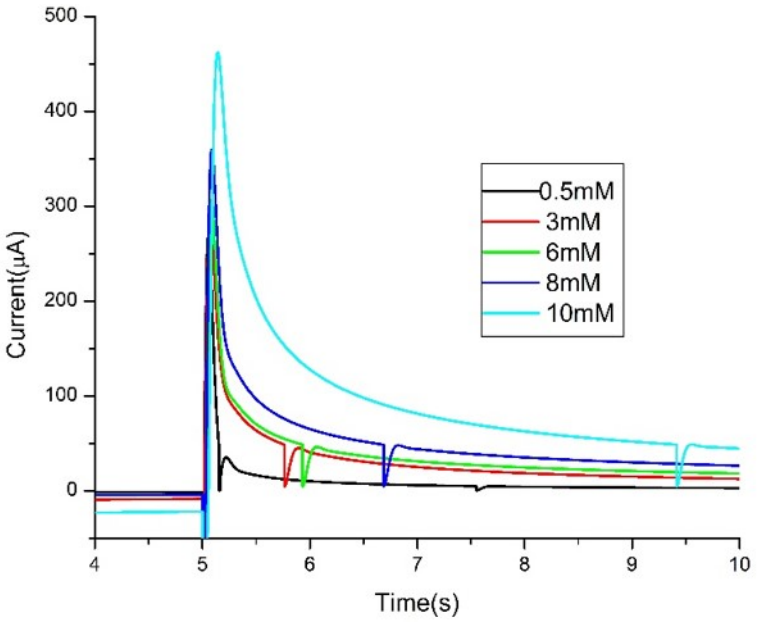

Figure 5.13: Chronoamperometric curves of different concentrations of $[Fe(CN)_6]^{3-/4-}$ measured by the prototype

sequently decreases the concentration gradient. In addition, the prototype recorded distinct faradaic currents that increased when the concentration of

the probe increased. Hence, the Cottrell equation can be applied to determine the diffusion coefficient of an electrochemical analyte and active surface area of the working electrode. In the calibration curve shown in Fig. 5.14 the prototype exhibited a good linearity for the concentration between 0.5 mM and 10 mM. The sensitivity of the device was 38 μA (per mM), which is relatively very high. The high sensitivity of the prototype is may be attributed

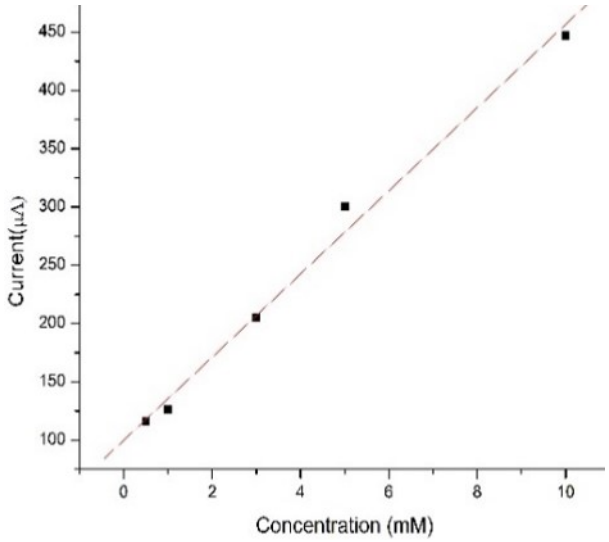

Figure 5.14: Calibration curve

to the larger area-to-volume ratio on the surface of the cluster assembled Au thin film working electrode. The larger effective active surface area of the cluster assembled electrode may provide the larger number of active sites for the oxidation of the electroactive species, which results in an increase of current. Therefore, the prototype manufactured by the combination of SCBD and FFF technologies can be potentially employed as a sensitive chronoamperometric sensor.

5.1.5 Electrochemical Impedance spectroscopy(EIS) characterization of the prototype of electrode embedded electrochemical microfluidic sensor

Nyquist impedance spectra measured using the prototype containing 10 mM of $[Fe(CN)_6]^{3-}/[Fe(CN)_6]^{4-}$ with the 1 M KNO_3 solution in the channel is presented in Fig. 5.15. The plot represents real and imaginary parts of the impedance of the electrochemical cell integrated into the microfluidics platform acquired for frequencies varying from 0.01 Hz to 10^6 Hz using the amplitude of 5 mV. Basically, different regions of the Nyquist spectra consist of the semi-circle and linear region where solution resistance(Rs), double layer capacitance(Cdl) and charge transfer resistance(Rct) is determined. However, in this case, the device recorded approximately linear complex spectra for both high and low-frequency regions without the semicircle in the mid-frequency region of the Nyquist plot. This response suggests the reaction was dominated by the diffusion process(mass-controlled), and the cluster assembled electrode exhibited very low polarization resistance, which illustrates that the electrode exhibited a fast charge transfer property.

It can also show cleanness of the film deposited on FFF printed ABS substrate. In addition, the high-frequency region displayed a linear tendency, with a slope smaller than 1, deviating from the ideal capacitive behavior. This behavior is explained by the constant phase element (CPE), which is related to the porosity of the electrode surface. In addition, a straight line inclined at a constant angle of 45 degrees appeared in the lower frequency range that indicates the existence of Warburg impedance, which represents

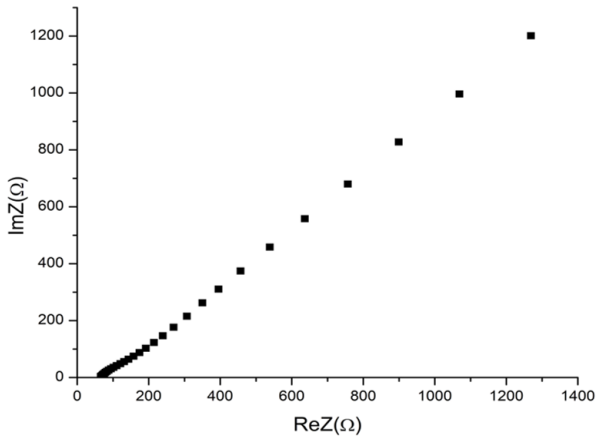

Figure 5.15: Nyquist plot of the impedance

semi-infinite diffusion of $[Fe(CN)_6]^{3-}/[Fe(CN)_6]^{4-}$ ions at the electrode solution interface. This response confirms the high roughness or porous structure of the cluster assembled thin films reported in [149]. The corresponding bode representations depicted in 5.16 clearly indicates the apparent dependence of the impedance on applied frequency. As it can be seen, in high-frequency regions, the slope is almost zero, indicating the frequency regions were dominated by the resistive behavior. In addition, the slope approaches zero value at low-frequency regions where the Rct is calculated. Also, the slope at mid-frequency region is found approximately -0.405, which deviates from ideal capacitive behavior where the slope is equal to -1. This deviation from ideal capacitive behavior may be attributed to the surface roughness or porosity nature of the cluster assembled thin films explained above.

Based on the information retrieved from the Nyquist and Bode the equivalent circuit representing the electrochemical interface of electrode and so-

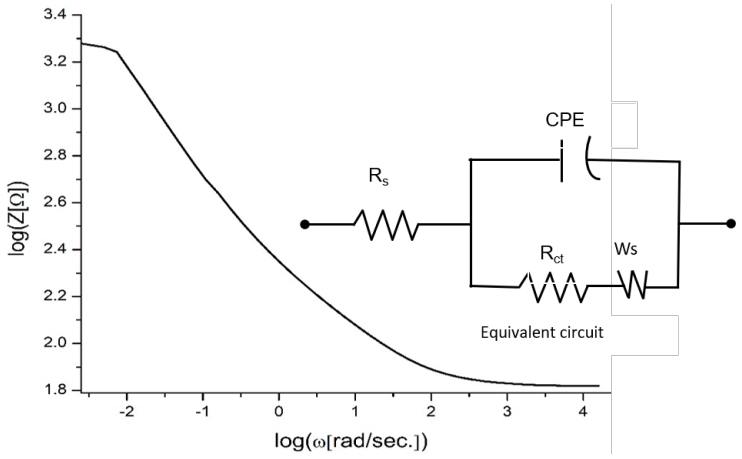

Figure 5.16: Bode plot representing logarithm of impedance versus logarithm of frequency

lution is established as presented in Fig. 5.16 inset, where CPE represents the property stem from the roughness and porosity of the cluster assembled electrode, Rs is the solution resistance, Rct is the charge transfer property of the electrode and Ws, the Warburg diffusion term at solution electrode interface. Thus, with a very high surface roughness and porous nature of cluster-assembled electrodes endowed by the SCBD, the prototype has a huge potential to be employed as a very sensitive electrochemical EIS sensor.

5.1.6 In channel flow hydrodynamic detection

In this part the prototype was assessed for its potential application in detection and analysis of analytes in continuously flowing solution. The laminar flow was introduced using kid scientific 100 syringe pump. The 10 mM ferro/ferricyanide in 1 M KNO_3 solution was pumped into the channel with varying flow rate through tubes joined to commercial connectors fitted to the inlet/outlet holes on the integrated system and cyclic voltammetry was recorded at different scan rates.

Fig. 5.17 shows current-voltage curve of 10 mM $[Fe(CN)_6]^{3-}/[Fe(CN)_6]^{4-}$ recorded using the newly manufactured electrode integrated electrochemical microfluidic sensor device at scan rate of 50 mV/S for various flow rates.

As can be seen, the curve displayed two peaks corresponding to oxidation and reduction potentials of $[Fe(CN)_6]^{3-}/[Fe(CN)_6]^{4-}$ redox couple for both flowing and quiescent solution. In addition, the flowing solution displayed flow rate dependent response. The limiting current recorded with low flow rate showed substantial increase as compared to the current recorded in the quiescent solution. The current increased when the flow rate increased up to 20 μL/s. This is due to the fact that at low scan rates increasing flow rate supplies fresh analytes to the Nernstian diffusion boundary consequently rendering additional mass transport means besides the diffusion occurring from the small stagnant region virtually close to surface of the electrode. The increase in the Faradic current transpires the successful introduction of addi-

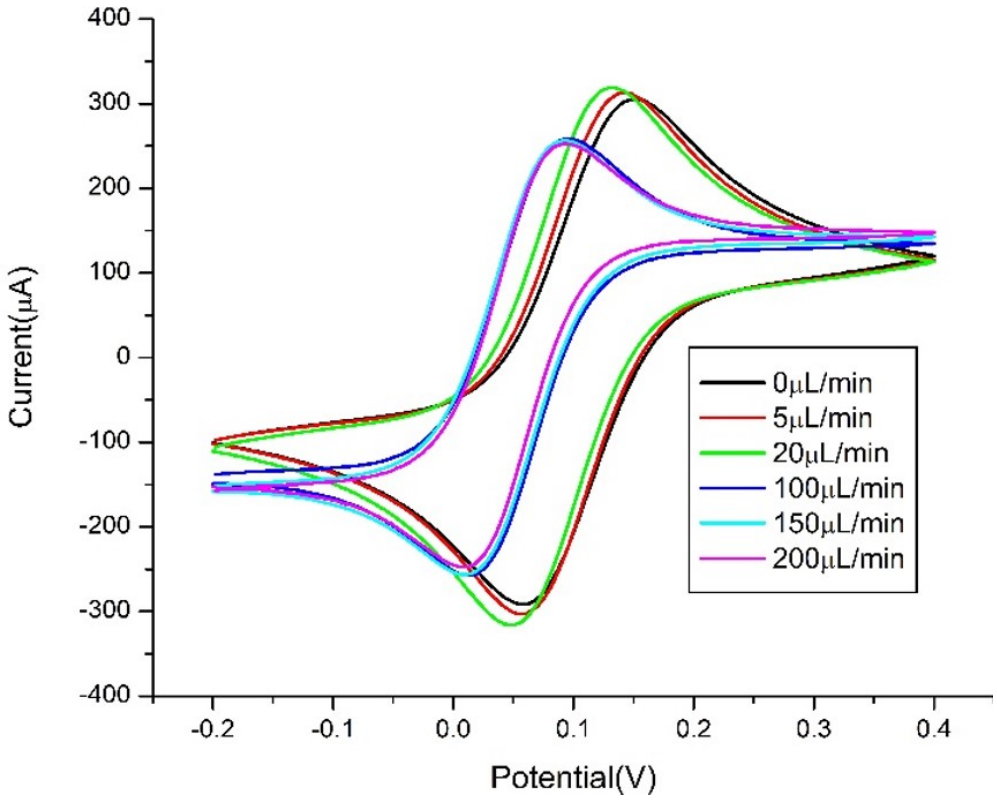

Figure 5.17: Cyclic voltammogram of 10 mM ferri/ferrocyanide scanned at 50 mV/S with different flow rates

tional mass transport to the electrode surface by convection. Hence, at low flow rates mass transport is controlled by both diffusion and convection of the electroactive species, thus increasing the flow rate increases peak current.

On the other hand, when the flow rate was increased beyond 100 μl/s the limiting current decreased, the voltammogram became sigmoidal, and the curve shifted to the left. In this case, the fast flowing stream does not permit more diffusion to occur and the scan rate is not quick enough to

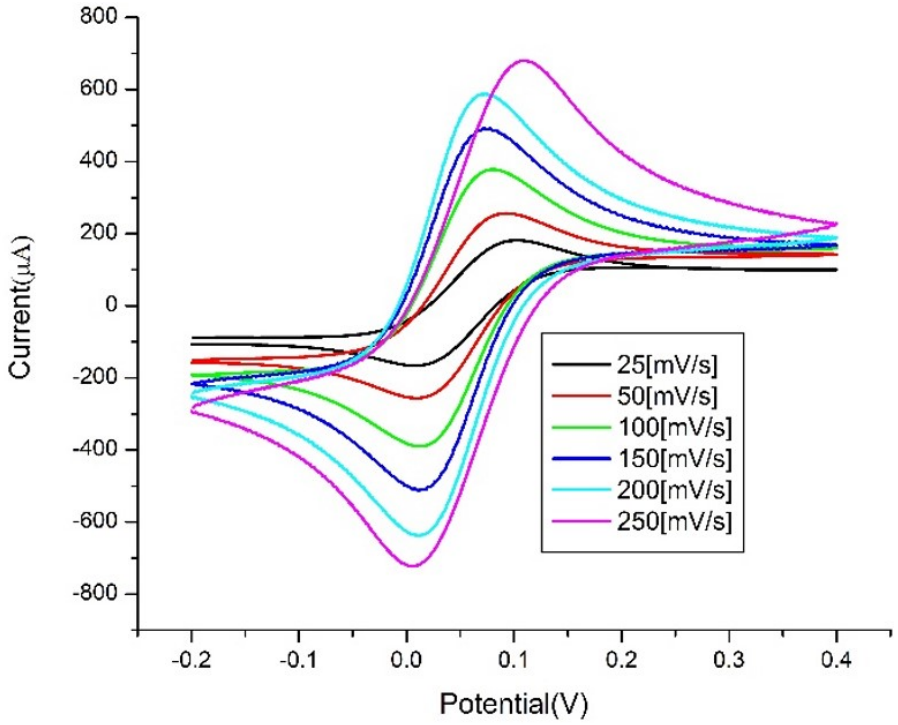

Figure 5.18: Voltammetric response of the integrated electrode sensing unit for 10 mM $[Fe(CN)_6]^{3-/4-}$ at 0.025-0.25 V/S for the flow rate of 300 μl/s

permit fast electron exchange as fresh analytes are supplied, and products are removed quickly by the convection resulting in a decreased limiting current. Accordingly, at high flow rates, the mass transport is controlled only by convection. The variation of limiting current with the scan rate for fixed high flow rate of 300 μl/s is shown in Fig. 5.18.

As clearly seen the voltammogram obtained at the scan rate of 25 mV/s is very narrow and sigmoidal than those obtained at higher scan rates. For the high scan rate of 250 mV/s increased oxidation limiting current was ob-

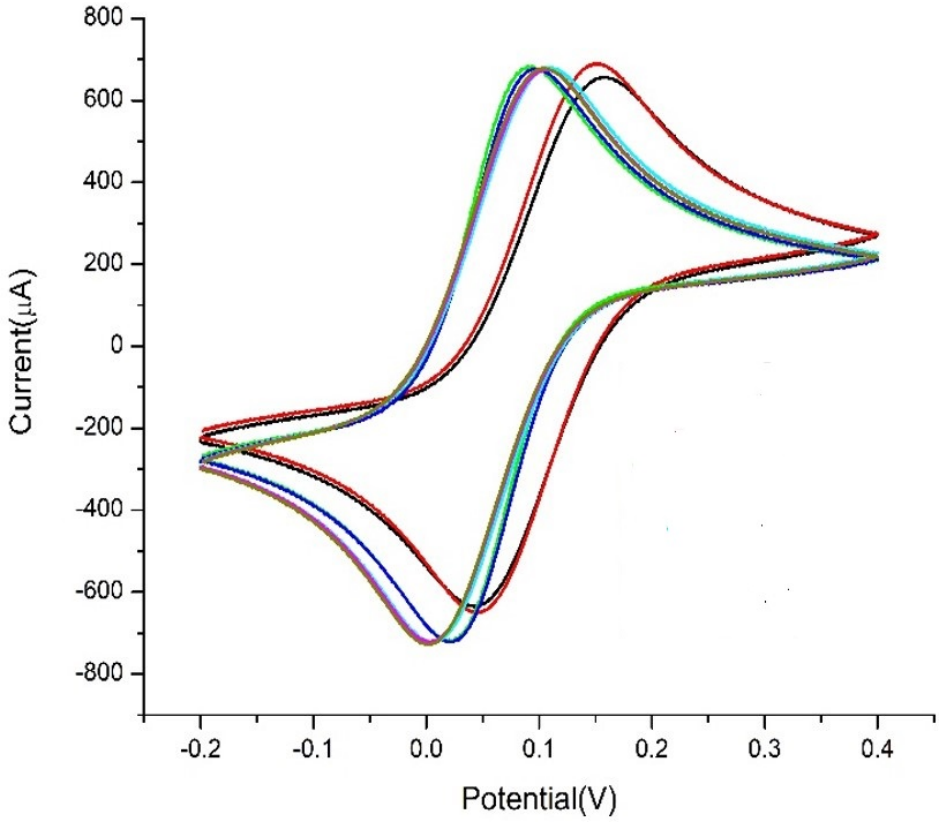

Figure 5.19: Voltammetric response of the integrated electrode sensing unit for 10 mM $[Fe(CN)_6]^{3-/4-}$ at the scan rate of 0.25 V/S for the flow rate of 300 μl/s

served for low flow rate, while no significant change was observed as the flow rate increased up to 300 μl/s. The peak current is virtually close that obtained in quiescent solution. This is because high scan rates are fast enough to consume fresh analytes continuously supplied by the convection and allow fast charge to transfer so that the limiting current did not diminish as clearly shown in Fig. 5.19.

As discussed in section 4.9, in laminar flow at steady state mass transport occurring to the electrode surface due to diffusion arises from the Nesrtian diffusion layer, which is normal to the stream. This diffusions layer is constant unlike in the case of quiescent solution that infinitely extends into the solution. The stream of flow brings analytes to the outer boundary of the Nernstian layer refilling the analytes consumed by the electrochemical reaction and consequently causing the diffusion layer to remain constant. This process enhances mass transport to the electrode surface by supplying flux of analytes from the bulk to the diffusion boundary close to the surface of electrodes. Accordingly, the mass transport equation is represented by the combined effect of both diffusion and convection[156, 157].

$$\frac{\partial[C_i]}{\partial t} - D_i \nabla^2 C_i + U \nabla C_i \tag{5.1}$$

where C_i is concentration and U is the stream velocity, $U\nabla C_i$ is the mass transfer introduced by convection. The laminar flow pattern on the electrode surface is obtained by adjusting the channel design and flow rate of the stream. In this case, streamlines that follow the velocity field do not cross each other and the small time independent diffusion layer is created σ distance from the surface is the electrode where mass transport occurs. This phenomena occurs perpendicular to the stream direction and represented by the second term in the equation 5.1. The mass transport to the diffusion regions boundary is carried tangential to the streamlines ad represented by the third term in the same equation.

For the electrode integrated microfluidics system satisfying the dimen-

sional relationship between the electrodes and channel, the current for steady state condition is given by equation 4.7. According to this equation the limiting current is related with cube root of flow rate. The introduction of flow into the electrochemical system renders additional means to deliver analyte to the diffusion region boundary. The increasing flux increases the limiting current if the scan rate allows fast transfer of electrons before it is washed away by the stream, which explains the increment of limiting current for low flow rate at the low scan rate. To the contrary, increasing the flow rate at low scan rate decreased the current. This is because fast stream of flow do not contribute flux the diffusion region for the fact that analytes are rapidly washed away before the electrochemical reaction consumes the delivered flux. In addition, fast streams wash away products formed at the boundary of diffusion region thereby denying the electrochemical charge transfer. High flow rate at low scan rate decreased the limiting current.

As the scan rate increased the effect of flow rate became insignificant. This is because fast scan rates allow the fast exchange of charge before they are washed away by the fast stream. As it can be seen in Fig. 5.19, no pronounced change in limiting current was observed when the solution was scanned at the scan rate of 0.25 $\frac{V}{s}$ for the higher flow rate of 300 $\frac{\mu L}{s}$

5.2 Summary

Three-electrodes embedded electrochemical microfluidic biosensors platform is successfully developed by integrating SCBD and FFF technologies via novel fabrication strategy. The fabrication strategy bridged the two-technology removing the limitation that has impeded leveraging of the FFF technology for manufacturing monotonically electrode integrated microfluidic biosensors. The fabrication strategy was cost-effective, flexible quick and do not require the cleanroom and trained technicians. Employing the strategy cost-effective, portable and user-friendly integrated electrochemical microfluidic biosensor platform was developed.

5.2.1 Manufacturing of electrode integrated electrochemical microfluidic biosensor platform

The flexibility in the manufacturing process of FFF technology that employs thermoplastics filament melts to additively manufacture the work-piece by localized material deposition enabled creating the window for integration of electrodes into FFF printed microfluidics platform. The two-step fabrication method enabled leveraging of consumer-grade Delta wasp FFF printer for fabrication of the desired device. Besides the low cost, FFF is employed for manufacturing end-use devices that can speed up the fabrication process. FFF raw materials are inexpensive and there is a broad range of production-grade thermoplastics available to make custom-based materials choice. Therefore, using FFF technology contributes enhanced fabrication pace, new functionality, reduced cost, and bench top fabrication process for

the development of integrated biosensor system.

The SCBD technology offered the possibility of deposition of nanostructured electrodes with tailored surface features on the thermoplastic substrates using gas phase cluster source. The nanostructured materials deposited on the plastics substrates are strongly anchored by implantation of metallic nanoparticles into the substrates matrix thereby metalizing plastic. The SCBD technology offered large area thin film deposition using focused and collimated beam generated by combining PMCS, supersonic expansion, and aerodynamic focusing. The metalization ability was leveraged to use FFF printed thermoplastic substrates for building electrochemical biosensors by depositing strongly anchored thin film electrodes. Besides, the surface tailoring ability was used for controlling the surface features of electrodes such as roughness and porosity thereby to enhance sensitivity and detection range. Because of the foregoing benefits, SCBD was used to couple with FFF technology through a novel integration strategy.

Cold acetone surface treatment process significantly reduced the roughness of FFF printed ABS substrates, which is the base material used in this project. The cold acetone treatment process reduced micro-surface roughness into nano-roughness thereby paving a way for utilization of FFF printed platforms.

Passivation of electrodes with acetoxy silicon adhesives successfully protected the electrodes from damage that could arise from overprinting pro-

cess to seal the channel. This strategy enables readily integration of FFF and SCBD technology for manufacturing electrode integrated microfluidic biosensor.

5.2.2 Electrochemical detection of ferro/ferricyanide

The prototype of three electrodes integrated electrochemical biosensors employed for detection of 10 mM ferro/ferricyanide probe in 1 M KNO_3 solution stagnant in a channel showed reversible and diffusion dependent electrochemical behavior of the probe when used as cyclic voltammetry electrochemical sensor. The highly sensitive electrochemical response was recorded when used as chronoamperometry sensor. The EIS measurement able to acquire qualitative information about the roughness and porous nature of the SCBD electrodes. The in channel flow analysis revealed that Faradic current increased as convection rate increased to 20 $\frac{\mu L}{s}$ and decreased when the convection rate further increased. This transpire that the device possess huge functionality for online or flow analysis.

Therefore, using the novel integration strategy the SCBD can be coupled with FFF technology and prevailing electrochemical fabrication methods to be employed for manufacturing scale-up of electrode embedded electrochemical microfluidics platform with the enhanced pace, portability and cost-efficient way. The integrated platform can be customized for developing various bio/chemical sensors.

5.2.3 Future perspective

The device has already showed a huge functionality as microfluidics on a chip chemical sensor in both stagnant and flowing solutions containing ferro/ferricynanide solution. Without any further modification the prototype device can be utilized to detect heavy metals traces such as lead, magnesium and cadmium using striping potential method. In addition, the device can be customized for detection of pesticides in stagnant and flow mood various.

To develop complete theoretical explanation for the flow analysis the device should be redesigned so that the dimension ration of electrode to channel satisfy the requisite for observation of pronounced current enhancement in flow analysis.

Bibliography

[1] Ming L., Honglei G, Israa AO. and Nianqiang W. Nanostructured Sensors for Detection of Heavy Metals: A Review. *CS Sustainable Chem. Eng.*, 2013, 1 (7), pp 713–723. DOI: 10.1021/sc400019a

[2] Sackmann, E. K., Fulton, A. L., & Beebe, D. J. (2014). The present and future role of microfluidics in biomedical research. *Nature. Nature Publishing Group*. https://doi.org/10.1038/nature13118

[3] Mairhofer, J., Roppert, K.,& Ertl, P. (2009, June). Microfluidic systems for pathogen sensing: A review. *Sensors (Switzerland)*. https://doi.org/10.3390/s90604804

[4] Chin, C. D., Linder, V., & Sia, S. K. (2007). Lab-on-a-chip devices for global health: Past studies and future opportunities. *Lab on a Chip. Royal Society of Chemistry*. https://doi.org/10.1039/b611455e

[5] Chand, R., & Neethirajan, S. (2017). Microfluidic platform integrated with graphene-gold nano-composite aptasensor for one-step detection of norovirus. *Biosensors and Bioelectronics*, 98, 47–53. https://doi.org/10.1016/j.bios.2017.06.026

[6] Tsopela, A., Laborde, A., Salvagnac, L., Ventalon, V., Bedel-Pereira, E., Séguy, I., ... Launay, J. (2016). Development of a lab-on-chip electrochemical biosensor for water quality analysis based on microalgal photosynthesis. *Biosensors and Bioelectronics*, 79, 568–573. https://doi.org/10.1016/j.bios.2015.12.050

[7] Hesari, N., Alum, A., Elzein, M.,& Abbaszadegan, M. (2016). A biosensor platform for rapid detection of E. coli in drinking water.*Enzyme and Microbial Technology* , 83, 22–28. https://doi.org/10.1016/j.enzmictec.2015.11.007

[8] Scognamiglio, V., Arduini, F., Palleschi, G., & Rea, G. (2014, November 1). Biosensing technology for sustainable food safety. *TrAC - Trends in Analytical Chemistry. Elsevier B.V.* https://doi.org/10.1016/j.trac.2014.07.007

[9] Jeong-Yeol, Y. ; Bumsang, K. ; Lab-on-a-Chip Pathogen Sensors for Food Safety. *Sensors* 2012, 12(8), 10713-10741; https://doi.org/10.3390/s120810713

[10] Neethirajan, S., Ragavan, K. V., & Weng, X. (2018, March 1). Agro-defense: Biosensors for food from healthy crops and animals. *Trends in Food Science and Technology. Elsevier Ltd.* https://doi.org/10.1016/j.tifs.2017.12.005

[11] Pundir, C. S., & Chauhan, N. (2012, October 1). Acetylcholinesterase inhibition-based biosensors for pesticide determination: A review. *Analytical Biochemistry*. https://doi.org/10.1016/j.ab.2012.06.025

[12] Justino, C.I.L.; Duarte, A.C.; Rocha-Santos, T.A.P.(2017). Recent progress in biosensors for environmental monitoring: A review.*Sensors* 17 2918; https://doi.org/10.3390/s17122918

[13] Medina-Sánchez M., Mayorga-Martinez C.C, Watanabe T., Ivandini T.T., Honda Y., Pino F., Nakata K., Fujishima A., Einaga Y., Merkoçi A. 2016 Microfluidic platform for environmental contaminants sensing and degradation based on boron-doped diamond electrodes, In *Biosensors and Bioelectronics*. 5, 365-374, doi:10.1016/j.bios.2015.08.058.

[14] Tan, H. Y., Loke, W. K., Nguyen, N. T., Tan, S. N., Tay, N. B., Wang, W., & Ng, S. H. (2014). Lab-on-a-chip for rapid electrochemical detection of nerve agent Sarin.*Biomedical Microdevices*, 16(2), 269–275. https://doi.org/10.1007/s10544-013-9830-4

[15] Kaushik, R., & Balasubramanian, R. (2013, January 1). Methods and approaches used for detection of cyanotoxins in environmental samples: A review. *Critical Reviews in Environmental Science and Technology*. https://doi.org/10.1080/10643389.2011.644224

[16] Noh, J., Kim, H. C., & Chung, T. D. (2011). Biosensors in microfluidic chips.*Topics in Current Chemistry*, 304, 117–152. https:/*doi.org*/10.1007/128_2011_143

[17] Sia, S. K., & Kricka, L. J. (2008). Microfluidics and point-of-care testing.*Lab on a Chip*, 8(12), 1982–1983. https://doi.org/10.1039/b817915h

[18] da Silva ETSG, Souto DEP, Barragan JTC, Giarola JF, de Moraes ACM, Kubota LT: Electrochemical biosensors in point-of-care devices: recent advances and future trends. *ChemElectroChem* 2017, 4:778–794

[19] Wooseok, J., Jungyoup, H., Jin-Woo C., Chong, HA. Point-of-care testing (POCT) diagnostic systems using microfluidic lab-on-a-chip technologies. *Microelectronic Engineering*, Volume 132, 25 January 2015, Pages 46-57.

[20] Chen, C., Wang, Y., Lockwood, S. Y., & Spence, D. M. (2014). 3D-printed fluidic devices enable quantitative evaluation of blood components in modified storage solutions for use in transfusion medicine. Analyst, 139(13), 3219–3226. https://doi.org/10.1039/c3an02357e

[21] Altintas, Z., Akgun, M., Kokturk, G., & Uludag, Y. (2018). A fully automated microfluidic-based electrochemical sensor for real-time bacteria detection. *Biosensors and Bioelectronics*, 100, 541–548. https://doi.org/10.1016/j.bios.2017.09.046

[22] Sameenoi Y., Koehler K., Shapiro J., Boonsong K., Sun Y., Collett J., Volckens Jr.J., and Henry C.S. 2012 Microfluidic Electrochemical Sensor for On-Line Monitoring of Aerosol Oxidative Activity, *Journal of the American Chemical Society* 134 (25), 10562-10568 doi: 10.1021/ja3031104.

[23] Pol, R., Céspedes, F., Gabriel, D., & Baeza, M. (2017, October 1). Microfluidic lab-on-a-chip platforms for environmental monitoring. *TrAC - Trends in Analytical Chemistry*. Elsevier B.V. https://doi.org/10.1016/j.trac.2017.08.001

[24] Newman, J. D., & Turner, A. P. F. (2005). Home blood glucose biosensors: A commercial perspective. Biosensors and Bioelectronics, 20(12), 2435–2453. https://doi.org/10.1016/j.bios.2004.11.012

[25] Jacobs, E., Vadasdi, E., Sarkozi, L., & Colman, N. (1993). Analytical evaluation of i-STAT Portable Clinical Analyzer and use by nonlaboratory health-care professionals. Clinical Chemistry, 39(6), 1069–1074.

[26] Pereira da Silva Neves, M. M., González-García, M. B., Hernández-Santos, D., & Fanjul-Bolado, P. (2018, August 1). Future trends in the market for electrochemical biosensing. *Current Opinion in Electrochemistry. Elsevier B.V.* https://doi.org/10.1016/j.coelec.2018.05.002

[27] https://www.idtechex.com/research/reports/biosensors-for-point-of-care-testingtechnologies-applications-forecasts-2017-2027-000553.asp(accessed 26.02.2018)

[28] https://www.marketresearchfuture.com/reports/electrochemical-biosensors-market2792 (accessed 27.03.2018)

[29] Prakash, S., Pinti, M., & Bhushan, B. (2012, May 28). Review article: Theory, fabrication and applications of microfluidic and nanofluidic biosensors. Philosophical Transactions of the Royal Society A: Mathematical, Physical and Engineering Sciences. Royal Society. https://doi.org/10.1098/rsta.2011.0498

[30] Chen, S., & Shamsi, M. H. (2017, July 20). Biosensors-on-chip: A topical review. *Journal of Micromechanics and Microengineering. Institute of Physics Publishing. https://doi.org/10.1088/1361-6439/aa7117*

[31] Luka, G., Ahmadi, A., Najjaran, H., Alocilja, E., Derosa, M., Wolthers, K., ... Hoorfar, M. (2015, December 1). Microfluidics integrated biosensors: A leading technology towards lab-on-A-chip and sensing applications.*Sensors (Switzerland)* . MDPI AG. https://doi.org/10.3390/s15122978

[32] Haeberle, S., Mark, D., Von Stetten, F., & Zengerle, R. (2012). Microfluidic platforms for lab-on-a-chip applications. *In Microsystems and Nanotechnology (Vol. 9783642182938, pp. 853–895). Springer-Verlag Berlin Heidelberg* https://*doi.org*/10.1007/978 − 3 − 642 − 18293 − $8_2$2

[33] Rackus, D. G., Shamsi, M. H., & Wheeler, A. R. (2015). Electrochemistry, biosensors and microfluidics: a convergence of fields. *Chemical Society Reviews*, 44(15), 5320–5340. https://doi.org/10.1039/c4cs00369a

[34] Merkoçi, A., Pumera, M., Llopis, X., Pérez, B., Del Valle, M., & Alegret, S. (2005, October). New materials for electrochemical sensing VI: Carbon nanotubes.*TrAC - Trends in Analytical Chemistry.* https://doi.org/10.1016/j.trac.2005.03.019

[35] Yi C.,Qingqiao W., Hongkun P.,Charles M. L. Nanowire Nanosensors for Highly Sensitive and Selective Detection of Biological and Chemical Species, Science 17 Aug 2001: Vol. 293, Issue 5533, pp. 1289-1292, DOI: 10.1126/science.1062711

[36] Campbell, M. G., & Dincă, M. (2017, May 12). Metal–organic frameworks as active materials in electronic sensor devices. *Sensors (Switzerland).* MDPI AG. https://doi.org/10.3390/s17051108

[37] Adhikari, B., & Majumdar, S. (2004). Polymers in sensor applications.*Progress in Polymer Science (Oxford)* , 29(7), 699–766. https://doi.org/10.1016/j.progpolymsci.2004.03.002

[38] Luo, X., Morrin, A., Killard, A. J., & Smyth, M. R. (2006, February). Application of nanoparticles in electrochemical sensors and biosensors. *Electroanalysis*. https://doi.org/10.1002/elan.200503415

[39] Solanki, P. R., Kaushik, A., Agrawal, V. V., & Malhotra, B. D. (2011, January). Nanostructured metal oxide-based biosensors. *NPG Asia Materials*. https://doi.org/10.1038/asiamat.2010.137

[40] Shao, Y., Wang, J., Wu, H., Liu, J., Aksay, I. A., & Lin, Y. (2010, May). Graphene based electrochemical sensors and biosensors: A review. *Electroanalysis*. https://doi.org/10.1002/elan.200900571

[41] Zhang, S., Wright, G., & Yang, Y. (2000). Materials and techniques for electrochemical biosensor design and construction. *Biosensors and Bioelectronics*, 15(5–6), 273–282. https://doi.org/10.1016/S0956-5663(00)00076-2

[42] Lee, J. H., Warner, C. M., Jin, H. E., Barnes, E., Poda, A. R., Perkins, E. J., & Lee, S. W. (2017). Production of tunable nanomaterials using hierarchically assembled bacteriophages.*Nature Protocols*, 12(9), 1999–2013. https://doi.org/10.1038/nprot.2017.085

[43] Iost, R. M., & Crespilho, F. N. (2012, January 15). Layer-by-layer self-assembly and electrochemistry: Applications in biosensing and bioelectronics. *Biosensors and Bioelectronics*. https://doi.org/10.1016/j.bios.2011.10.040

[44] Hu, Y., Huang, Y., Tan, C., Zhang, X., Lu, Q., Sindoro, M., ... Zhang, H. (2017). Two-dimensional transition metal dichalcogenide nanomaterials for biosensing applications. *Mater. Chem. Front.*, 1(1), 24–36. https://doi.org/10.1039/C6QM00195E

[45] Yang, M., Qu, F., Lu, Y., He, Y., Shen, G., & Yu, R. (2006). Platinum nanowire nanoelectrode array for the fabrication of biosensors. *Biomaterials,* 27(35), 5944–5950. https://doi.org/10.1016/j.biomaterials.2006.08.014

[46] McDonald, J. C., Duffy, D. C., Anderson, J. R., Chiu, D. T., Wu, H., Schueller, O. J., & Whitesides, G. M. (2000). Fabrication of microfluidic systems in poly(dimethylsiloxane). *Electrophoresis,* 21(1), 27–40. https://doi.org/10.1002/(SICI)1522-2683(20000101)21:1¡27::AID-ELPS27¿3.0.CO;2-C

[47] Tsao, C. W. (2016). Polymer microfluidics: Simple, low-cost fabrication process bridging academic lab research to commercialized production. *Micromachines*. MDPI AG. https://doi.org/10.3390/mi7120225

[48] Ali, M. A., Srivastava, S., Solanki, P. R., Reddy, V., Agrawal, V. V., Kim, C., ... Malhotra, B. D. (2013). Highly efficient bienzyme functionalized nanocomposite-based microfluidics biosensor platform for biomedical application. *Scientific Reports*, 3. https://doi.org/10.1038/srep02661

[49] Ren, K., Chen, Y., & Wu, H. (2014, February). New materials for microfluidics in biology. *Current Opinion in Biotechnology*. https://doi.org/10.1016/j.copbio.2013.09.004

[50] Aura, S., Sikanen, T., Kotiaho, T., & Franssila, S. (2008). Novel hybrid material for microfluidic devices. *Sensors and Actuators, B: Chemical,* 132(2), 397–403. https://doi.org/10.1016/j.snb.2007.10.007

[51] Tsougeni, K., Tserepi, A., & Gogolides, E. (2007). Photosensitive poly(dimethylsiloxane) materials for microfluidic applications. *Microelectronic Engineering,* 84(5–8), 1104–1108. https://doi.org/10.1016/j.mee.2007.01.011

[52] Nunes, P. S., Ohlsson, P. D., Ordeig, O., & Kutter, J. P. (2010, August). Cyclic olefin polymers: Emerging materials for lab-on-a-chip applications. *Microfluidics and Nanofluidics*. https://doi.org/10.1007/s10404-010-0605-4

[53] Domachuk, P., Tsioris, K., Omenetto, F. G., & Kaplan, D. L. (2010, January 12). Bio-microfluidics: Biomaterials and biomimetic designs.*Advanced Materials.* https://doi.org/10.1002/adma.200900821

[54] Nie, J., Zhang, Y., Lin, L., Zhou, C., Li, S., Zhang, L., & Li, J. (2012). Low-Cost Fabrication of Paper-Based Micro fluidic Devices by One- Step Plotting. *Anal. Chem.,* 84, 6331–6335. https://doi.org/10.1021/ac203496c

[55] Lakard, B., Jeannot, J. C., Spajer, M., Herlem, G., De Labachelerie, M., Blind, P., & Fahys, B. (2005). Fabrication of a miniaturized cell using microsystem technologies for electrochemical applications. *Electrochimica Acta,* 50(9), 1863–1869. https://doi.org/10.1016/j.electacta.2004.08.038

[56] Pimpin, A., & Srituravanich, W. (2012). Reviews on micro- and nanolithography techniques and their applications. *Engineering Journal.* https://doi.org/10.4186/ej.2012.16.1.37

[57] Becker, H., & Gärtner, C. (2000). Polymer microfabrication methods for microfluidic analytical applications. Electrophoresis. Wiley-VCH Verlag. https://doi.org/10.1002/(SICI)1522-2683(20000101)21:1¡12::AID-ELPS12¿3.0.CO;2-7

[58] Mohammed, M. I., Zainal Alam, M. N. H., Kouzani, A., & Gibson, I. (2017). Fabrication of microfluidic devices: improvement of surface quality of CO 2 laser machined poly(methylmethacrylate) polymer. *Journal of Micromechanics and Microengineering*, 27(1), 015021. https://doi.org/10.1088/0960-1317/27/1/015021

[59] Moolman MC, Huang Z, Krishnan ST, Kerssemakers JW, Dekker NH. 2013 Electron beam fabrication of a microfluidic device for studying submicron-scale bacteria. *Journal of Nanobiotechnology.*11, 12. Doi: 10.1186/1477-3155-11-12

[60] Tsao, C. W., & DeVoe, D. L. (2009). Bonding of thermoplastic polymer microfluidics. Microfluidics and Nanofluidics. https://doi.org/10.1007/s10404-008-0361-x

[61] Hou, X., Zhang, Y. S., Santiago, G. T. D., Alvarez, M. M., Ribas, J., Jonas, S. J., ... Khademhosseini, A. (2017, April 20). Interplay between materials and microfluidics. *Nature Reviews Materials. Nature Publishing Group.* https://doi.org/10.1038/natrevmats.2017.16

[62] Ren, K., Zhou, J., & Wu, H. (2013). Materials for microfluidic chip fabrication. *Accounts of Chemical Research*, 46(11), 2396–2406. https://doi.org/10.1021/ar300314

[63] Mark, D., Haeberle, S., Roth, G., Von Stetten, F., & Zengerle, R. (2010). Microfluidic lab-on-a-chip platforms: Requirements, characteristics and applications. *NATO Science for Peace and Security Series A: Chemistry and Biology*. https://doi.org/10.1007/978-90-481-9029-4-17

[64] Xia, Y., & Whitesides, G. M. (1998). Soft Lithography. *Angewandte Chemie International Edition*, 37(5), 550–575. https://doi.org/10.1002/(SICI)1521-3773(19980316)37:5¡550::AID-ANIE550¿3.3.CO;2-7

[65] Sia, S. K., & Whitesides, G. M. (2003, November). Microfluidic devices fabricated in poly(dimethylsiloxane) for biological studies. *Electrophoresis*. https://doi.org/10.1002/elps.200305584

[66] Pataky, K., & Brugger, J. (2014). Rapid prototyping techniques for the fabrication of biosensors. In Rapid Prototyping of Biomaterials: Principles and Applications (pp. 75–96). *Elsevier Ltd*. https://doi.org/10.1533/9780857097217.75

[67] Waldbaur A, Rapp H, Länge K and Rapp B. E., 2011 Let there be chip–towards rapid prototyping of microfluidic devices: *one-step manufacturing processes Anal*. Methods 3 2681–716. DOI:10.1039/C1AY05253E

[68] O'Neill, P. F., Ben Azouz, A., Vázquez, M., Liu, J., Marczak, S., Slouka, Z., ... Brabazon, D. (2014). Advances in three-dimensional rapid proto-

typing of microfluidic devices for biological applications. *Biomicrofluidics*, 8(5). https://doi.org/10.1063/1.4898632

[69] He, Y., Wu, Y., Fu, J. Z., Gao, Q., & Qiu, J. J. (2016, August 1). Developments of 3D Printing Microfluidics and Applications in Chemistry and Biology: a Review. *Electroanalysis. Wiley-VCH Verlag.* https://doi.org/10.1002/elan.201600043

[70] Manzanares Palenzuela, C. L., & Pumera, M. (2018, June 1). (Bio)Analytical chemistry enabled by 3D printing: Sensors and biosensors. TrAC - Trends in Analytical Chemistry. *Elsevier B.V.* https://doi.org/10.1016/j.trac.2018.03.016

[71] Barborini, E., Piseri, P., & Milani, P. (1999). Pulsed microplasma source of high intensity supersonic carbon cluster beams. *Journal of Physics D: Applied Physics*, 32(21). https://doi.org/10.1088/0022-3727/32/21/102

[72] P. Milani, P. Piseri, and E. Barborini, Cluster beam synthesis of nanostructured thin films, *Journal of Vacuum Science & Technology* A 19, 2025 (2001); https://doi.org/10.1116/1.1331289

[73] Borghi, F., Melis, C., Ghisleri, C., Podestà, A., Ravagnan, L., Colombo, L., & Milani, P. (2015). Stretchable nanocomposite electrodes with tunable mechanical properties by supersonic cluster beam implantation in elastomers. Applied Physics Letters, 106(12). https://doi.org/10.1063/1.4916350

[74] Ghisleri, C., Borghi, F., Ravagnan, L., Podestà, A., Melis, C., Colombo, L., & Milani, P. (2014). Patterning of gold-polydimethylsiloxane (Au-

PDMS) nanocomposites by supersonic cluster beam implantation. *Journal of Physics D: Applied Physics*, 47(1). https://doi.org/10.1088/0022-3727/47/1/015301

[75] Ravagnan, L., Divitini, G., Rebasti, S., Marelli, M., Piseri, P., & Milani, P. (2009). Poly(methyl methacrylate)-palladium clusters nanocomposite formation by supersonic cluster beam deposition: A method for microstructured metallization of polymer surfaces.*Journal of Physics D: Applied Physics*, 42(8). https://doi.org/10.1088/0022-3727/42/8/082002

[76] Ahn, D., Kweon, J. H., Kwon, S., Song, J., & Lee, S. (2009). Representation of surface roughness in fused deposition modeling. Journal of Materials Processing Technology, 209(15–16), 5593–5600. https://doi.org/10.1016/j.jmatprotec.2009.05.016

[77] McCullough, E. J., & Yadavalli, V. K. (2013). Surface modification of fused deposition modeling ABS to enable rapid prototyping of biomedical microdevices. Journal of Materials Processing Technology, 213(6), 947–954. https://doi.org/10.1016/j.jmatprotec.2012.12.015

[78] Thèvenot, D. R., Toth, K., Durst, R. A., & Wilson, G. S. (2001). Electrochemical biosensors: Recommended definitions and classification. *Biosensors and Bioelectronics*, 16(1–2), 121–131. https://doi.org/10.1016/S0956-5663(01)00115-4

[79] Grieshaber, D., MacKenzie, R., Vörös, J., & Reimhult, E. (2008). Electrochemical biosensors - *Sensor principles and architectures. Sensors.* MDPI AG. https://doi.org/10.3390/s8031400

[80] Bard, A. J., Faulkner, L. R., York, N., @bullet, C., Brisbane, W., & Toronto, S. E. (1944). ELECTROCHEMICAL METHODS Fundamentals and Applications. Electrochemistry. I. Faulkner, Larry R (pp. 3–7). https://doi.org/10.1016/B978-0-12-381373-2.00056-9

[81] Zhang, S., Wright, G., & Yang, Y. (2000). Materials and techniques for electrochemical biosensor design and construction. *Biosensors and Bioelectronics*, 15(5–6), 273–282. https://doi.org/10.1016/S0956-5663(00)00076-2

[82] Waleed Shinwari, M., Zhitomirsky, D., Deen, I. A., Selvaganapathy, P. R., Jamal Deen, M., & Landheer, D. (2010, March). Microfabricated reference electrodes and their biosensing applications. *Sensors*. https://doi.org/10.3390/s100301679

[83] Sindre S., Erik A. J., Frode S., Kristin I., Long-term stability of screen-printed pseudo-reference electrodes for electrochemical biosensors,*Electrochimica Acta*, Volume 287, 2018, Pages 29-36, https://*doi.org*/10.1016/*j.electacta*.2018.08.045

[84] Meng L., Yuan-Ting L., Da-Wei L., Yi-Tao L. Recent developments and applications of screen-printed electrodes in environmental assays—A review, *Analytica Chimica Acta*, Volume 734, 2012, Pages 31-44. https://doi.org/10.1016/j.aca.2012.05.018

[85] Inzelt, G., Lewenstam, A., & Scholz, F. (2013). Handbook of reference electrodes. Handbook of Reference Electrodes (pp. 1–344). Springer Berlin Heidelberg. https://doi.org/10.1007/978-3-642-36188-3

[86] . Soleymani, L., Fang, Z., Sargent, E. H., & Kelley, S. O. (2009). Programming the detection limits of biosensors through controlled nanostructuring. *Nature Nanotechnology*, 4(12), 844–848. https://doi.org/10.1038/nnano.2009.27

[87] Zhu, C., Yang, G., Li, H., Du, D., & Lin, Y. (2015, January 6). Electrochemical sensors and biosensors based on nanomaterials and nanostructures. *Analytical Chemistry. American Chemical Society.* https://doi.org/10.1021/ac5039863

[88] Gleiter, H. (2000). Nanostructured materials: basic concepts and microstructure. *Acta Materialia*, 48(1), 1–29. https://doi.org/10.1016/S1359-6454(99)00285-2

[89] Walcarius, A., Minteer, S. D., Wang, J., Lin, Y., & Merkoçi, A. (2013). Nanomaterials for bio-functionalized electrodes: Recent trends. *Journal of Materials Chemistry B*, 1(38), 4878–4908. https://doi.org/10.1039/c3tb20881h

[90] Moriarty, P. (2001). Nanostructured materials. *Reports on Progress in Physics*, 64(3), 297–381. https://doi.org/10.1088/0034-4885/64/3/201

[91] Francesca B., Bianca S., Costanza P., Paolo M. and Alessandro A.Electrostatic Double-Layer Interaction at the Surface of Rough Cluster-Assembled Films: The Case of Nanostructured Zirconia. Langmuir, 34,35, 10230-10242, 2018, doi = 10.1021/acs.langmuir.8b01387

[92] Singh, A. V., Ferri, M., Tamplenizza, M., Borghi, F., Divitini, G., Ducati, C., ... Milani, P. (2012). Bottom-up engineering of the surface

roughness of nanostructured cubic zirconia to control cell adhesion. Nanotechnology, 23(47). https://doi.org/10.1088/0957-4484/23/47/475101

[93] Borghi, F., Vyas, V., Podestà, A., & Milani, P. (2013). Nanoscale Roughness and Morphology Affect the IsoElectric Point of Titania Surfaces. PLoS ONE, 8(7). https://doi.org/10.1371/journal.pone.0068655

[94] Wiederrecht, G. (2010).*Handbook of Nanofabrication*. Academic Press (pp. 183–208).

[95] Maduraiveeran, G., Sasidharan, M., & Ganesan, V. (2018, April 30). Electrochemical sensor and biosensor platforms based on advanced nanomaterials for biological and biomedical applications. *Biosensors and Bioelectronics. Elsevier Ltd*. https://doi.org/10.1016/j.bios.2017.12.031

[96] Hakim, M. M. A., Lombardini, M., Sun, K., Giustiniano, F., Roach, P. L., Davies, D. E., ... Ashburn, P. (2012). Thin film polycrystalline silicon nanowire biosensors.*Nano Letters*, 12(4), 1868–1872. https://doi.org/10.1021/nl2042276

[97] Li, H., Liu, S., Dai, Z., Bao, J., & Yang, X. (2009, November). Applications of nanomaterials in electrochemical enzyme biosensors. *Sensors*. https://doi.org/10.3390/s91108547

[98] Byun, I., Coleman, A. W., & Kim, B. (2013). Transfer of thin Au films to polydimethylsiloxane (PDMS) with reliable bonding using (3-mercaptopropyl)trimethoxysilane (MPTMS) as a molecular adhesive. *Journal of Micromechanics and Microengineering*, 23(8). https://doi.org/10.1088/0960-1317/23/8/085016

[99] Loo, Y. L., Willett, R. L., Baldwin, K. W., & Rogers, J. A. (2002). Additive, nanoscale patterning of metal films with a stamp and a surface chemistry mediated transfer process: Applications in plastic electronics. *Applied Physics Letters*, 81(3), 562–564. https://doi.org/10.1063/1.1493226

[100] Wei, D. (2010). Electrochemical nanofabrication. Nanotechnology (pp. 3–50). https://doi.org/10.4032/9789814303743

[101] Li, M., Li, Y. T., Li, D. W., & Long, Y. T. (2012, July 13). Recent developments and applications of screen-printed electrodes in environmental assays-A review. *Analytica Chimica Acta*. https://doi.org/10.1016/j.aca.2012.05.018

[102] Wu, J., Wang, R., Yu, H., Li, G., Xu, K., Tien, N. C., ... Li, D. (2015). Inkjet-printed microelectrodes on PDMS as biosensors for functionalized microfluidic systems. *Lab on a Chip*, 15(3), 690–695. https://doi.org/10.1039/c4lc01121j

[103] Mohtashim S. & Sensen C. (2017) Biosensors-on-Chip: A Topical Review. *Journal of Micromechanics and Microengineering*. 27. 083001-083017. 10.1088/1361-6439/aa7117.

[104] Whitesides, G. M. (2006, July 27). The origins and the future of microfluidics.*Nature*. https://doi.org/10.1038/nature05058

[105] Manz, A., Widmers, H. M., & Graber, N. (1990). Miniaturized total chemical analysis systems: A novel concept for chemical sensing. *Sensors and Actuators B*: Chemical, 1(1–6), 244–248. https://doi.org/10.1016/0925-4005(90)80209-I

[106] Siontorou, C. G., Bratakou, S., Karapetis, S., & Tzamtzis, N. (2018). Biosensors Based on Microfluidic Devices Lab-on-a-Chip and Microfluidic Technology. *Nanotechnology and Biosensors*, 375–394. https://doi.org/10.1016/B978-0-12-813855-7.00013-1

[107] Squires, T. M., & Quake, S. R. (2005). Microfluidics: Fluid physics at the nanoliter scale. Reviews of Modern Physics, 77(3), 977–1026. https://doi.org/10.1103/RevModPhys.77.977

[108] Stone, H. A., Stroock, A. D., & Ajdari, A. (2004). ENGINEERING FLOWS IN SMALL DEVICES. Annual Review of Fluid Mechanics, 36(1), 381–411. https://doi.org/10.1146/annurev.fluid.36.050802.122124

[109] Liu, D., & Garimella, S. V. (2004). Investigation of liquid flow in microchannels. Journal of Thermophysics and Heat Transfer, 18(1), 65–72. https://doi.org/10.2514/1.9124

[110] Whitesides, G. M., & Stroock, A. D. (2001). Flexible methods for microfluidics. Physics Today, 54(6), 42. https://doi.org/10.1063/1.1387591

[111] Chhabra R. and Shankar, V. Chapter 6 - Transport Processes in Microfluidic Applications. In Coulson and Richardson's Chemical Engineering (pp. 529 - 546). https://doi.org/10.1016/B978-0-08-102550-5.00006-7

[112] Adesokan, B. J., Quan, X., Evgrafov, A., Sørensen, M. P., Heiskanen, A., & Boisen, A. (2014). Hydrodynamics studies of cyclic voltammetry for electrochemical micro biosensors. *In Journal of Physics: Conference Series (Vol. 574). Institute of Physics Publishing.* https://doi.org/10.1088/1742-6596/574/1/012008

[113] Saem, S.; Zhu, Y.; Luu, H.; Moran-Mirabal, J. Bench-Top Fabrication of an All-PDMS Microfluidic Electrochemical Cell Sensor Integrating Micro/Nanostructured Electrodes. *Sensors* 2017, 17, 732.

[114] Duffy, D. C., McDonald, J. C., Schueller, O. J. A., & Whitesides, G. M. (1998). Rapid prototyping of microfluidic systems in poly(dimethylsiloxane). Analytical Chemistry, 70(23), 4974–4984. https://doi.org/10.1021/ac980656z

[115] Ghaderinezhad, F., Amin, R., Temirel, M., Yenilmez, B., Wentworth, A., & Tasoglu, S. (2017). High-throughput rapid-prototyping of low-cost paper-based microfluidics. Scientific Reports, 7(1). https://doi.org/10.1038/s41598-017-02931-6

[116] Young, E. W. K., Berthier, E., Guckenberger, D. J., Sackmann, E., Lamers, C., Meyvantsson, I., ... Beebe, D. J. (2011). Rapid prototyping of arrayed microfluidic systems in polystyrene for cell-based assays. Analytical Chemistry, 83(4), 1408–1417. https://doi.org/10.1021/ac102897h

[117] Kim, J., Kim, J., Shin, Y., Song, S.,& Lee, J. (2014). Rapid prototyping of multifunctional microfluidic cartridges for electrochemical biosensing platforms. Sensors and Actuators, B: Chemical, 202, 60–66. https://doi.org/10.1016/j.snb.2014.05.009F

[118] Gibson, I., Rosen, D., & Stucker, B. (2015). Additive Manufacturing Technologies. Additive Manufacturing Technologies: 3D Printing, Rapid Prototyping, and Direct Digital Manufacturing, Second Edition (pp. 1–498). https://doi.org/10.1007/978-1-4939-2113-3

[119] Dutse, S. W., & Yusof, N. A. (2011). Microfluidics-based lab-on-chip systems in DNA-based biosensing: An overview. *Sensors*, 11(6), 5754–5768. https://doi.org/10.3390/s110605754

[120] Rusling, J. F. (2018). Developing Microfluidic Sensing Devices Using 3D Printing. ACS Sensors, 3(3), 522–526. https://doi.org/10.1021/acssensors.8b00079

[121] Melchels, F. P. W., Feijen, J., & Grijpma, D. W. (2010, August). A review on stereolithography and its applications in biomedical engineering. *Biomaterials*. https://doi.org/10.1016/j.biomaterials.2010.04.050

[122] Hull, C. W. (1986). Apparatus for production of three-dimensional objects by stereolithography. US Patent 4,575,330, 1–16. https://doi.org/10.1145/634067.634234.

[123] Rogers, C. I., Qaderi, K., Woolley, A. T., & Nordin, G. P. (2015). 3D printed microfluidic devices with integrated valves. Biomicrofluidics, 9(1). https://doi.org/10.1063/1.4905840

[124] Au, A. K., Lee, W., & Folch, A. (2014). Mail-order microfluidics: Evaluation of stereolithography for the production of microfluidic devices. Lab on a Chip, 14(7), 1294–1301. https://doi.org/10.1039/c3lc51360b

[125] Sankaran, V. P., Dubey, S., Sharma, A., Agarwal, A., & Goel, S. (2017). Stereolithographic 3D Printed Microfluidic Viscometer for Rapid Detection of Automobile Fuel Adulteration. Sensor Letters, 15(7), 545–551. https://doi.org/10.1166/sl.2017.3848

[126] Erkal, J. L., Selimovic, A., Gross, B. C., Lockwood, S. Y., Walton, E. L., McNamara, S., ... Spence, D. M. (2014). 3D printed microfluidic devices with integrated versatile and reusable electrodes. Lab on a Chip, 14(12), 2023–2032. https://doi.org/10.1039/c4lc00171k

[127] Ji, Q., Zhang, J. M., Liu, Y., Li, X., Lv, P., Jin, D., & Duan, H. (2018). A Modular Microfluidic Device via Multimaterial 3D Printing for Emulsion Generation. Scientific Reports, 8(1). https://doi.org/10.1038/s41598-018-22756-1

[128] Anderson, K. B., Lockwood, S. Y., Martin, R. S., & Spence, D. M. (2013). A 3D printed fluidic device that enables integrated features. *Analytical Chemistry*, 85(12), 5622–5626. https://doi.org/10.1021/ac4009594

[129] Gibson, I., & Shi, D. P. (1997). Material properties and fabrication parameters in selective laser sintering process. Rapid Prototyping Journal, 3(4), 129–136. https://doi.org/Doi 10.1108/13552549710191836

[130] Ziemian, C. W., & Iii, P. M. C. (2001). Computer aided decision support for fused deposition modeling. *Rapid Prototyping Journal*, 7(3), 138–147. https://doi.org/10.1108/13552540110395538

[131] Masood, S. H. (2014). Advances in Fused Deposition Modeling. In Comprehensive Materials Processing (Vol. 10, pp. 69–91). Elsevier Ltd.

[132] Chudobova, D., Cihalova, K., Skalickova, S., Zitka, J., Rodrigo, M. A. M., Milosavljevic, V., ... Kizek, R. (2015). 3D-printed chip for detection of methicillin-resistant Staphylococcus au-

reus labeled with gold nanoparticles. Electrophoresis, 36(3), 457–466. https://doi.org/10.1002/elps.201400321

[133] Comina, G., Suska, A., & Filippini, D. (2014). Low cost lab-on-a-chip prototyping with a consumer grade 3D printer. *ab on a Chip*, 14(16), 2978–2982. https://doi.org/10.1039/c4lc00394b

[134] Kadimisetty, K., Malla, S., & Rusling, J. F. (2017). Automated 3-D Printed Arrays to Evaluate Genotoxic Chemistry: E-Cigarettes and Water Samples. *ACS Sensors*, 2(5), 670–678. https://doi.org/10.1021/acssensors.7b00118

[135] Salentijn, G. I. J., Oomen, P. E., Grajewski, M., & Verpoorte, E. (2017). Fused Deposition Modeling 3D Printing for (Bio)analytical Device Fabrication: Procedures, Materials, and Applications. Analytical Chemistry, 89(13), 7053–7061. https://doi.org/10.1021/acs.analchem.7b00828

[136] Yuen, P. K. (2016). Embedding objects during 3D printing to add new functionalities. Biomicrofluidics, 10(4). https://doi.org/10.1063/1.4958909

[137] Novakova-Marcincinova, L., & Kuric, I. (2012). Basic and Advanced Materials for Fused Deposition Modeling Rapid Prototyping Technology. Manuf. and Ind. Eng, 11(1), 1338–6549.

[138] Thomas, D., & Gilbert, S. (2014). Costs and Cost Effectiveness of Additive Manufacturing - A Literature Review and Discussion. NIST Special Publication, 1176, 1–77. https://doi.org/10.6028/NIST.SP.1176

[139] Boparai, K. S., Singh, R., & Singh, H. (2016). Development of rapid tooling using fused deposition modeling: A review. Rapid Prototyping

Journal. Emerald Group Publishing Ltd. https://doi.org/10.1108/RPJ-04-2014-0048

[140] Gowers, S. A. N., Curto, V. F., Seneci, C. A., Wang, C., Anastasova, S., Vadgama, P., ... Boutelle, M. G. (2015). 3D Printed Microfluidic Device with Integrated Biosensors for Online Analysis of Subcutaneous Human Microdialysate. Analytical Chemistry, 87(15), 7763–7770. https://doi.org/10.1021/acs.analchem.5b01353

[141] Dickinson, E. J. F., Streeter, I., & Compton, R. G. (2008). Theory of chronoamperometry at cylindrical microelectrodes and their arrays. *Journal of Physical Chemistry C*, 112(31), 11637–11644. https://doi.org/10.1021/jp801867e

[142] Lasia, A. (2014). Electrochemical Impedance Spectroscopy and its Applications. *Zeitschrift für Physikalische Chemie* (Vol. 29, pp. 287–288). https://doi.org/10.1007/978-1-4614-8933-7

[143] Henley, I. E., Yunus, K., & Fisher, A. C. (2003). Voltammetry under microfluidic control: Computer-aided design development and application of novel microelectrochemical reactors. *Journal of Physical Chemistry B*, 107(16), 3878–3884. https://doi.org/10.1021/jp022533v

[144] Chen, C., Wang, Y., Lockwood, S. Y., & Spence, D. M. (2014). 3D-printed fluidic devices enable quantitative evaluation of blood components in modified storage solutions for use in transfusion medicine. *Analyst*, 139(13), 3219–3226. https://doi.org/10.1039/c3an02357e

[145] Damiati, S. ,Küpcü, S., Peacock, M., Eilenberger,C., Zamzami,M., Qadri,I., Choudhry,H. Sleytr, U. B., and Schuster, B. Acoustic and hybrid 3D-printed electrochemical biosensors for the real-time immunodetection of liver cancer cells (HepG2) *Biosens. Bioelectron.*, 2017, 94, 500–506. https://doi.org/10.1016/j.bios.2017.03.045

[146] Krejcova, L., Nejdl, L., Rodrigo, M. A. M., Zurek, M., Matousek, M., Hynek, D., ... Kizek, R. (2014). 3D printed chip for electrochemical detection of influenza virus labeled with CdS quantum dots. Biosensors and Bioelectronics, 54, 421–427. https://doi.org/10.1016/j.bios.2013.10.031

[147] Vlachova, J., Tmejova, K., Kopel, P., Korabik, M., Zitka, J., Hynek, D., ... Kizek, R. (2015). A 3D microfluidic chip for electrochemical detection of hydrolysed nucleic bases by a modified glassy carbon electrode. Sensors (Switzerland), 15(2), 2438–2452. https://doi.org/10.3390/s150202438

[148] Bishop, G. W., Satterwhite, J. E., Bhakta, S., Kadimisetty, K., Gillette, K. M., Chen, E., & Rusling, J. F. (2015). 3D-Printed fluidic devices for nanoparticle preparation and flow-injection amperometry using integrated prussian blue nanoparticle-modified electrodes. *Analytical Chemistry*, 87(10), 5437–5443. https://doi.org/10.1021/acs.analchem.5b00903

[149] Borghi, F., Podestà, A., Piazzoni, C., & Milani, P. (2018). Growth Mechanism of Cluster-Assembled Surfaces: From Sub-monolayer to Thin-Film Regime. Physical Review Applied, 9(4). https://doi.org/10.1103/PhysRevApplied.9.044016

[150] Barborini, E., Piseri, P., Li Bassi, A., Ferrari, A. C., Bottani, C. E., & Milani, P. (1999). Synthesis of carbon films with controlled nanostructure by separation of neutral clusters in supersonic beams. Chemical Physics Letters, 300(5–6), 633–638. https://doi.org/10.1016/S0009-2614(98)01449-3

[151] Barborini, E., Piseri, P., Podesta, A., & Milani, P. (2000). Cluster beam microfabrication of patterns of three-dimensional nanostructured objects. Applied Physics Letters, 77(7), 1059–1061. https://doi.org/10.1063/1.1289040

[152] Piseri, P., Podestà, A., Barborini, E., & Milani, P. (2001). Production and characterization of highly intense and collimated cluster beams by inertial focusing in supersonic expansions. Review of Scientific Instruments, 72(5), 2261–2267. https://doi.org/10.1063/1.1361082

[153] Schwarzacher, W. (2006). Electrodeposition: A Technology for the Future. The Electrochemical Society Interface, 15(1), 32–35.

[154] Kissinger, P. T., & Heineman, W. R. (1983). Cyclic Voltammetry. Journal of Chemical Education, 60(9), 702–710. https://doi.org/10.1016/0165-9936(94)87010-1

[155] Pohanka, M., & Republic, C. (2008). Electrochemical biosensors–principles and applications. Methods, 6(2), 57–64. *http* : *//www.zsf.jcu.cz/jab/*6_2*/pohanka.pdf*

[156] Adesokan, B. J., Quan, X., Evgrafov, A., Heiskanen, A., Boisen, A., & Sørensen, M. P. (2016). Experimentation and numerical modeling of cyclic

voltammetry for electrochemical micro-sized sensors under the influence of electrolyte flow. Journal of Electroanalytical Chemistry, 763, 141–148. https://doi.org/10.1016/j.jelechem.2015.12.029

[157] Compton, R. G., Fisher, A. C., Geoffrey Wellington, R., Dobson, P. J., & Leigh, P. A. (1993). Hydrodynamic voltammetry with microelectrodes. Channel microband electrodes: Theory and experiment. Journal of Physical Chemistry, 97(40), 10410–10415. https://doi.org/10.1021/j100142a024